The effects of highly reduced magmatism revealed through aubrites

Zoë E. Wilbur[1,2,3*], Arya Udry[2], Francis M. McCubbin[4], Kathleen E. Vander Kaaden[3,5], Christopher DeFelice[2], Karen Ziegler[6], Daniel Kent Ross[3**], Timothy J. McCoy[6], Juliane Gross[4,8], Jessica J. Barnes[1], Nick Dygert[9], Ryan A. Zeigler[4], Brent D. Turrin[8], Christopher McCoy[2]

[1]Lunar and Planetary Laboratory, University of Arizona, Tucson, AZ, USA
[2]University of Nevada, Las Vegas, Las Vegas, NV, USA
[3]Jacobs, NASA Johnson Space Center, Mail Code XI3, Houston, TX, USA
[4]NASA Johnson Space Center, Mailcode XI, Houston, TX 77058, USA
[5]NASA Headquarters, Mary W. Jackson Building, Washington, D.C., USA
[6]Department of Mineral Sciences, National Museum of Natural History, Smithsonian Institution, Washington, DC, USA
[7]Institute of Meteoritics, Department of Earth and Planetary Sciences, University of New Mexico, Albuquerque, NM, USA
[8]Department of Earth and Planetary Science, Rutgers State University of New Jersey, NJ, USA
[9]Department of Earth and Planetary Sciences, University of Tennessee, TN, USA

*Corresponding author E-mail: zewilbur@email.arizona.edu
**This work was released posthumously

Abstract – Enstatite-rich meteorites, including the aubrites, formed under conditions of very low oxygen fugacity (fO_2: Iron Wüstite buffer –2 to –6), and thus offer the ability to study reduced magmatism present on multiple bodies in our solar system. Elemental partitioning among metals, sulfides, and silicates is poorly constrained at low fO_2; however, studies of enstatite-rich meteorites may yield empirical evidence of the effects of low fO_2 on elemental behavior. This work presents comprehensive petrologic and oxygen isotopic studies of 14 aubrites, including four meteorites that have not been previously investigated in detail. The aubrites exhibit a variety of textures and mineralogy, and their elemental zoning patterns point to slow cooling histories for all 14 samples. Oxygen isotope analyses suggest that the aubrite parent bodies may be more heterogeneous than originally reported or may have experienced incomplete magmatic differentiation. Contrary to the other classified aubrites and based on textural and mineralogical observations, we suggest that the Northwest Africa 8396 meteorite shows an affinity for an enstatite chondrite parentage. By measuring major elemental compositions of silicates, sulfides, and metals, we calculate new metal-silicate, sulfide-silicate, and sulfide-metal partition coefficients for aubrites that are applicable to igneous systems at low fO_2. The geochemical behavior of elements in aubrites, as determined using partition coefficients, is similar to the geochemical behavior of elements determined experimentally for magmatic systems on Mercury. Enstatite-rich meteorites, including aubrites, represent valuable natural petrologic analogous to Mercury and their study could further our understanding of reduced magmatism in our solar system.

INTRODUCTION

The aubrites are a subset of enstatite-rich meteorites that originate from differentiated bodies (e.g., Keil, 2010). Enstatite-rich meteorites are unique samples characterized by extremely low oxygen fugacities (fO_2) that range from 2 to 6 log units below the Iron-Wüstite (IW) buffer (e.g., Keil 1968, 2010), making these meteorites the most reduced rocks in the sample collection (Larimer and Buseck, 1974; Brett and Sato, 1984; Fogel, 1998; Chabot and Drake, 1999; Barrat et al., 2016). At such low fO_2, lithophile elements can behave as chalcophile (sulfur-loving) or siderophile (iron-loving) elements (e.g., McCubbin et al., 2012; McCoy and Bullock, 2017; Vander Kaaden et al., 2017). These different elemental affinities can lead to the formation of sulfide and phosphide minerals that are not typically observed in more oxidized systems, like Earth. Elemental partitioning in these exotic, reduced magmatic systems are poorly constrained (e.g., McCubbin et al., 2012; Vander Kaaden et al., 2017; McCubbin et al., 2017; McCoy and Bullock, 2017). Specifically, there is very limited data from natural and experimental systems regarding how moderately volatile elements partition between sulfide, silicate, and metallic phases in reduced magmas (e.g., McCoy et al., 1999; Bouhifd et al., 2007; Vander Kaaden and McCubbin, 2016; Boujibar et al., 2019; Steentra et al., 2020a, 2020b, 2020c). Systematically studying enstatite-rich meteorites, like aubrites, allows us to better constrain elemental partitioning on parent bodies that formed at reducing conditions.

Aubrites are a rare group of differentiated enstatite-rich meteorites (80 samples listed in the meteorite collection per the Meteoritical Bulletin, and only ~30 samples including pairings) that formed by igneous processes. Aubrites are represented by fragmental breccias, regolith breccias, and unbrecciated rocks (e.g., Keil, 2010). Their mineralogy is dominated by FeO-poor enstatite and minor forsterite, diopside, plagioclase, troilite (FeS), and Fe,Ni metal. Aubrites also contain rare sulfides in trace abundances that may reflect the unique elemental partitioning in their extremely reducing conditions of formation. Some of these rare sulfides are daubréelite [$FeCr_2S_4$], oldhamite [(Ca,Mg)S], alabandite [(Mn,Fe)S], caswellsilverite [$NaCrS_2$], heideite [$FeTi_2S_4$], and djerfisherite [$K_6Na(Fe,Cu,Ni)_{25}S_{26}Cl$] (Watters and Prinz, 1979; Keil, 2010; McCoy and Bullock, 2017). Many of these sulfides are unique to meteorites. However, there are terrestrial examples of oldhamite (found in Disko Island Greenland) and djerfisherite (found in the Koashva Open Pit Apatite Mine in Russia) present in reduced localities on Earth (Piatak et al., 2012; Ebel and Sack, 2013). The aubrites are suggested to have originated on parent bodies of enstatite-chondrite like precursors (e.g., Keil, 2010; McCoy and Bullock, 2017).

A comprehensive petrologic and geochemical study of aubrites is imperative to better constrain the formation of reduced magmas in our solar system. Here we conduct petrographic, mineral major element composition, 3D X-ray computed tomography, bulk chemical, and oxygen isotope analyses on 14 aubrites to better constrain the formation of aubrites, including four samples that have not been described in detail previously: LaPaz Icefield (LAP) 02233, Miller Range (MIL) 07008, MIL 13004, and Northwest Africa (NWA) 8396. By conducting a systematic study of a representative subset of the aubrite suite, we aim to better define the elemental partitioning in reduced parent bodies, including Mercury. The mineralogy and oxygen fugacities of aubrites are similar to the inferred mineralogy and fO_2 at the mercurian surface that was estimated from data collected by the MESSENGER (MErcury Surface, Space ENvironment, GEochemistry, and Ranging) spacecraft (e.g., McCubbin et al., 2017; Namur and Charlier, 2017; Vander Kaaden et al., 2017; McCoy et al., 2018). Previously, the geochemical compositions of enstatite chondrite impact melts were compared to Mercury, however these rocks do not originate from a

differentiated body (Udry et al., 2019). Thus, aubrites may represent valuable analogs for further experimental and mission-related mercurian studies.

SAMPLES AND ANALYTICAL TECHNIQUES

Samples

This study reports data from 14 aubrites of variable textures and degrees of brecciation, which are representative of the entire aubrite suite. Table 1 lists the samples studied in this work, including the number of thin sections analyzed, their degree of brecciation, their source, and the analyses conducted on each thin section. This study includes LAP 02233, MIL 07008, MIL 13004, and NWA 8396, which have not been previously investigated in detail. Some samples have been thoroughly studied previously (e.g., Bishopville, Cumberland Falls, Norton County, Peña Blanca Spring, ALH 78113 and Shallowater; Keil, 1968; Kimura et al., 1993; Keil 2010). We do not aim to reevaluate the petrogenesis of these rocks, but have analyzed them in order to characterize a representative subset of aubrites and to determine the geochemical behavior of elements in a large suite of aubrite samples in a self-consistent way. Reporting new analyses of previously studied samples enables inter-laboratory comparisons with other studies for assessment of any inter-laboratory biases.

Electron Probe Microanalyses

Major and minor element compositions of silicate, sulfide, phosphide, and metal phases within the aubrite meteorite samples were conducted using the *JEOL* JXA–8530F Electron microprobe (EMP) at NASA's Johnson Space Center (JSC). Conditions of 15 keV, 15 nA, and a phi-rho-z (PRZ) correction (Merlet, 1994) were used for the silicates, and conditions of 15 keV, 20 nA, and a ZAF correction (Castaing, 1951; utilizing the atomic number, absorption, and fluorescence correction factors) were used for the sulfide, metal, and phosphide phases. Phases were analyzed with a spot size of 5 μm, except for much smaller grains analyzed with a focused beam of 1 μm. The following information outlines the EMP standards used at JSC. The feldspar standards included: albite (for analysis of Si, Al, Na), orthoclase (Si, Al, K), anorthite (Si, Al, Ca), rutile (Ti), olivine (Fe, Mg), chromite (Cr), and rhodonite (Mn). For pyroxenes and olivines, the standards used were: olivine (Mg, Si, Fe), rhodonite (Mn), rutile (Ti), anorthite (Al), diopside (Ca), apatite (P), orthoclase (K), Ni metal (Ni), and tugtupite (Cl). The sulfides were standardized using: tugtupite (Cl), rutile (Ti), albite (Na), olivine (Mg), silicon metal (Si), apatite (P, Ca), orthoclase (K), troilite (S), chromite (Cr), rhodonite (Mn), Fe metal (Fe), Cu metal (Cu), Zn metal (Zn), and Ni metal (Ni). For silicate analyses, peak count times of 60 seconds and background count times of 30 seconds were used for Cl, Ti, Na, K, Cr, Mn, Fe, and Ni. Peak count times of 30 seconds and background count times of 15 seconds were used for Mg, Ca and Si. Peak count times of 40 seconds and background count times of 20 seconds were used for P and Al. For sulfide, phosphide, and metal analyses, peak count times of 40 seconds and background count times of 20 seconds were used for Cl, Ti, Si, P, Cr, Cu, Zn, and Mn. Peak count times of 60 seconds and background count times of 30 seconds were used for Na, Ni, and K whereas, peak count times of 30 seconds and background count times of 15 seconds were used for and Mg, S, Ca, and Fe (see Supplementary Table S1 for detection limits). Analyses of mineral compositions were accepted based on appropriate stoichiometry for the phase, and for totals between 98 to 101.5 wt.% for most minerals.

Quantification of Modal Mineralogy

Modal abundances (vol.%) were obtained using *ImageJ* software by employing pixel count analyses of Mg, Fe, Ca, Al, Si, Cr, S, Na, Ti, Ni, and P X-ray maps, which were obtained by WDS mapping using the *JEOL* JXA–8900 EMP at the University of Nevada, Las Vegas (UNLV) and EDS (energy dispersive X-ray spectroscopy) mapping using the JXA–8530F EMP at JSC. The X-ray elemental maps were collected at 15 keV and 50 nA at UNLV and 15 keV and 30 nA at JSC. The mineral modes are considered to be the volume abundance of each phase in the thin section and were calculated as the sum of pixels for each mineral as a percentage of all assigned pixels, where epoxy and unassigned pixels are omitted (McCubbin et al., 2021). A maximum error of ~5% was estimated for the modal abundance calculations determined with the supervised image classification technique (Maloy and Treiman, 2007). During replication of the digital extraction of phases, we found a minimum error of 2.3% and a maximum error of 7.2% for all phases.

Inductively Coupled Plasma-Mass Spectrometry (ICP-MS)

Bulk element abundances were determined with a *Thermo Scientific* iCAP Qc quadrupole ICP-MS at UNLV. The following elements were measured: Sc, V, Cr, Mn, Co, Ni, Cu, Zn, Rb, Sr, Y, Zr, Nb, Ba, La, Ce, Pr, Nd, Sm, Eu, Gd, Tb, Dy, Ho, Er, Tm, Yb, Lu, Hf, Ta, Pb, Th, and U. Fifty to one hundred milligrams of sample were dissolved in acid-cleaned Savillex beakers in a 1:1 mixture of sub-boiled double distilled HNO_3 and Optima grade HF. The samples were heated in concentrated, double distilled HF:HNO_3 mixture (3:1) on a hot plate at 100°C for two weeks to a month. No undissolved residual sample was observed in any of the beakers. The beakers were then opened, and the dissolution mixture was dried down. Once dry, 1 ml of 50% double distilled nitric acid was added and allowed to dry down. This step was repeated three times. Then, samples were rehydrated in 6 ml of 50% HNO_3, and then diluted by a factor of ~5000 for analysis. The samples were diluted with 2% nitric acid that was made with ultra-pure Millipore water (18 MΩ•cm). Samples were prepared with rock standards BHVO-1, BHVO-2, BCR-1, and AGV-1, as well as total procedural blanks at a similar dilution factor as the samples. The four rock standards were all used in a linear calibration curve for concentration calculations. Reproducibility of the reference materials was generally better than 5% (relative standard deviation – RSD). The long-term reproducibility and uncertainty of analyses is tested by running the USGS standard BHVO-2 as an unknown. The same analytical sequence as Huang and Frey (2003) was followed and the same standard concentrations were used.

Laser Fluorination – Oxygen Isotopic Analysis

Oxygen isotope analyses were performed by laser fluorination at the University of New Mexico (Sharp, 1990). Samples were gently crushed, and samples large enough (0.2 to 2 mg) were hand-picked for CO_2 laser-fluorination dual inlet mass spectrometry. Three subsamples were measured per meteorite. Samples were leached by using 6N HCl to remove possible terrestrial weathering products. Filled Ni sample plates were placed in the vacuum chamber of the instrument, pumped under high vacuum, and heated by a heat lamp for a minimum of 24 hours at room temperature to completely outgas the samples and remove potential moisture. Samples were then pre-fluorinated (BrF_5) to clean the stainless-steel system and to react residual traces of water or air in the fluorination chamber. Molecular oxygen was released from the samples by laser-assisted fluorination (50 W infrared CO_2 laser) in a ~100 mb BrF_5-atmosphere, producing molecular O_2 gas, SiF_4 gas, and solid fluorides. Excess reagent and gaseous SiF_4 were separated

from O_2 by reaction with hot NaCl and cryogenic trapping at –196°C. The oxygen was purified by freezing onto a 13 Å molecular sieve at –196°C, followed by elution of the O_2 from the first sieve at ~300°C into a He-stream that carries the oxygen through a gas chromatograph (GC) column (separation of O_2 and NF_3, a possible interference with the ^{17}O measurement) to a second 13 Å molecular sieve at −196°C. After removal of the He, the O_2 was then released directly into a dual inlet isotope ratio mass spectrometer (Thermo Finnigan MAT 253 Plus). The oxygen isotope ratios were calibrated against the isotopic composition of San Carlos olivine (Pack et al., 2016). Each sample analysis consists of 20 cycles of sample–standard comparison and olivine standards (~1–2 mg) were analyzed daily. Oxygen isotopic ratios were calculated using the following procedure: The $\delta^{18}O$ values refer to the per–mil deviation in a sample ($^{18}O/^{16}O$) from standard mean ocean water (SMOW), expressed as $\delta^{18}O = [(^{18}O/^{16}O)\ \text{sample}/(^{18}O/^{16}O)\ \text{SMOW}–1] \times 10^3$. The delta-values are converted to linearized prime values by calculating: $\delta^{18}O/^{17}O' = \ln[(\delta^{18}O/^{17}O + 10^3)/10^3] \times 10^3$ in order to create mass–fractionation curves. The $\Delta^{17}O'$ values were obtained from the linear δ-values by the following relationship: $\Delta^{17}O' = \delta^{17}O' – 0.528 \times \delta^{18}O'$, $\Delta^{17}O'$ values of zero define the terrestrial mass-fractionation line. $\Delta^{17}O'$ values lying on any line with a slope of ~0.52–0.53 are due to mass-dependent processes. Typical analytical precision of the laser–fluorination technique is better than ± 0.01‰ for $\Delta^{17}O$, as determined with duplicates.

X-Ray Computed Tomography

The Cumberland Falls, Mount Egerton, Norton County, Peña Blanca Spring, and Shallowater aubrites were scanned using X-ray computed tomography (XCT) to produce a 3D representation of the meteorites' textures and structures, and to calculate phase/mineral modal abundances. A *Nikon* XTH 320 micro-XCT system at NASA JSC was used. The samples were scanned using a 225 kV rotating target reflection source, with a resolution of 14.3–55.7 microns/voxel. Scans were conducted using a 2 mm copper filter. The XCT scan conditions are available in Supplementary Material Table S2. The 2D images, or "slices," from the scans were processed with *CT Agent Pro 3D* software to create a 3D rendering, and modal abundances were calculated using the 3D data by segmenting a density histogram in *Volume Graphics Studio* software. This software operates by assigning gray values to minerals, and these gray values correspond to the minerals' electron densities and chemical compositions, known as their linear attenuation coefficients (LAC). The peaks in the density histogram corresponding to different gray values were discernable and were separated based on local minimums. According to the evaluation of reproducibility of digital data extraction methods by Freidrich et al. (2008), the error of 3D modal mineralogy by XCT is 6%. This error represents an upper limit (Freidrich et al., 2021). The total rock volumes were computed using *Dragonfly* software, where the whole rock was segmented and isolated from the surrounding air and measured for total volume.

^{39}Ar-^{40}Ar

We used an $^{40}Ar/^{39}Ar$ step-heating method to evaluate ages of crystallization for Bishopville at two laboratories (Rutgers University – RU and Arizona State University – ASU), following methods as described in Udry et al. (2019), for the RU data. Analyses of Bishopville conducted at ASU were as follows: Multiple grains of Bishopville were packed in Al foil, loaded into Al discs, stacked in a flame-sealed glass vial, and irradiated for 100 hours. Samples were fused with a Photon Machines 55W CO_2 laser. Isotope data were collected using a Nu Instruments Nobelesse multi-collector mass spectrometer. Average backgrounds ± standard deviations from

blank runs were used to correct isotope abundances. An assumed solar $^{40}Ar/^{36}Ar$ value of 1 was used to correct the data for mass discrimination. Age data were reduced using the decay constant of 5.543×10^{-10} a^{-1} (Steiger and Jager, 1977). Isotope data were corrected for blank, radioactive decay, mass discrimination and interfering reactions. Cosmogenic corrections were applied using a cosmogenic $^{38}Ar/^{36}Ar$ of 1.54 (Weiler, 2002) and a solar $^{38}Ar/^{36}Ar$ of 0.187 (Nier, 1950). Age uncertainties are reported at the 2σ level.

RESULTS

Petrography

Reflected light and cross polarized light images of the studied aubrites are displayed in Figure 1. Backscattered electron images of phases in the meteorites are shown in Figure 2. X-ray image elemental composites of selected aubrites are displayed in Figure 3. The modal abundances presented in this section refer to Table 2. While we have studied half the classified aubrite suite, we only describe the most recent samples added to the collection and/or the lesser studied aubrites below. For a summary of aubrite petrography, see Keil (2010) and references therein.

Allan Hills (ALH) 78113: This aubrite is a fragmental breccia composed of discrete, subhedral enstatite (95 vol.%) measuring up to 6 mm in size, surrounded by a matrix of comminuted enstatite (Fig. 3a). Forsterite (1.0 vol.%) and trace albite and diopside (all measuring up to 0.6 mm in size) are present as discrete grains within the enstatitic matrix. A single Fe,Ni metal grain containing schreibersite [$(Fe,Ni)_3P$] that is mostly confined to the edges of the metal grain (Fig. 1a) as well as metal grains containing daubréelite inclusions (Fig. 2a–b) were observed. The sulfide assemblages consist of troilite in contact with daubréelite, alabandite, and djerfisherite. Although the sulfides are usually found dispersed in the enstatite matrix, some sulfides are found in contact with forsterite grains. Iron- and Ca-rich weathering products are present within cracks in the enstatite.

Allan Hills (ALH) 84007: This aubrite is a fragmental breccia composed of a matrix of comminuted enstatite (96 vol.%). Irregular-shaped, discrete grains of forsterite, plagioclase, and diopside are present in trace amounts within the matrix. Metal, daubréelite, troilite with daubréelite exsolution lamellae (1.2 vol.%), and alabandite with rounded daubréelite (Fig. 1b), occur in contact with each other in assemblages that measure up to 1.5 mm in length. Metal (0.5 vol.%) is present as discrete grains and is found in contact with troilite and daubréelite. Schreibersite is present at the edges of metal grains. Djerfisherite (Fig. 2c) was observed at the edges of composite sulfide grains.

LaPaz (LAP) 02233: This meteorite is non-brecciated and is composed almost entirely of enstatite (99 vol.%; Fig. 3c). The enstatite is observed as coarse, heavily shocked aggregates (see Rubin, 2015 for explanation of shock effects). Small angular grains of diopside (0.2 vol.%) are present within the enstatite matrix. Discrete grains of weathered troilite (up to 100 μm) and daubréelite (up to 50 μm) are present. The sulfides in this sample are surrounded by secondary Fe,Mn-rich phases that were likely produced by weathering.

Larkman Nunatak (LAR) 04316: This sample is a regolith breccia (determined from solar wind implanted gases; see Keil et al., 2011, and references therein) composed of large, angular enstatite (97 vol.%) in a matrix of smaller enstatite grains (Fig. 1c; Fig. 3d). Several of the larger enstatite grains exhibit diopside exsolution lamellae or shock induced polysynthetic

twinning, and diopside is also present as individual grains (1.1 vol.%). Forsterite (5.8 vol.%) is angular and exhibits Ca-rich veins. Plagioclase grains (4.7 vol.%) are angular and have exsolution lamellae. Troilite (0.8 vol.%) is observed in contact with daubréelite and alabandite (Fig. 2d). Metal grains, up to 300 μm in length, are surrounded by an Fe-rich weathering product.

Miller Range (MIL) 07008: This aubrite is a fragmental breccia composed of rounded and angular enstatite (95 vol.%) in a matrix of Na-rich quenched melt (1.8 vol.%) and comminuted enstatite (Fig. 3e). Forsterite (2.3 vol.%) is present as discrete grains and as chadacrysts within enstatite oikocrysts. Sulfide and metal grains in the sample measure up to 100 microns in length. Alabandite and troilite are the most abundant sulfide phases (Fig. 2e). Fe,Ni metal and Ca-rich alteration phases form veinlets within the glassy matrix.

Miller Range (MIL) 13004: This aubrite is brecciated and is composed of angular enstatite (92 vol.%) in a matrix of smaller enstatite grains (Fig. 3f). Olivine grains (4.0 vol.%) up to 800 μm are rounded, and some are chadacrysts within mm-sized enstatite oikocrysts (Fig. 1d). Albitic plagioclase (2.8 vol.%), albitic glass, and trace diopside are present. Troilite is observed in association with oldhamite. Ferroan alabandite and caswellsilverite typically occur together in this sample. An altered Cr-Na-bearing sulfide is observed in contact with alabandite. This phase is potentially schöllhornite [$Na_{0.3}(H_2O)CrS_2$], an alteration phase of caswellsilverite. Heidite is present in fractures (Fig. 2f).

Northwest Africa (NWA) 8396: This sample is composed of equigranular enstatite cut by Fe-and Ca-rich terrestrial weathering veins (Fig. 2g; Fig. 3g). Plagioclase (8 vol.%), troilite (3.6 vol.%), and metal (1.7 vol.%) grains are anhedral and surrounded by weathering veins (Fig. 2h). Trace daubréelite occurs in association with troilite, and most troilite grains contain daubréelite exsolution lamellae. Many plagioclase grains contain rounded enstatite, troilite, and daubréelite as inclusions. Ca-rich, rounded, weathered material is present around sulfide and metal.

Impact Melt: Impact melts were observed within Bishopville, Cumberland Falls, and LAR 04316 (Fig. 4). The melt in Bishopville and LAR 04316 exhibits a schlieren texture (Fig. 4a, 4b, 4d), while the melt in Cumberland Falls is included within an enstatite grain (Fig. 4c). The impact melt in these samples contains spherules primarily composed of Fe and S (measured via EDS).

3D modal mineralogy

The 3D modal mineralogical results from the XCT scans are outlined in Table 3 and Figure 5 (see supplementary data for CT scan conditions and videos of Mt Egerton, Cumberland Falls, and Norton County). We were able to distinguish silicates and groundmass (49 cm^{-1} peak), metal (64 cm^{-1} peak), and sulfides (i.e., troilite; 29 cm^{-1} peak) by segmenting a density histogram (Hanna and Ketcham, 2017). The phases are distinguished based upon their theoretical linear attenuation coefficients (LAC), which were calculated using a MuCalc spreadsheet of LAC values (Hanna and Ketcham, 2017). By creating a region of interest with the selected grey values for each group of phases that were distinguishable, it was possible to calculate aubrite 3D modal mineralogy. In the case of Shallowater, we were able to differentiate weathering veins and calculate a 3D abundance of Fe- and Ca-rich weathered phases. Compared to the 2D modal mineralogy (Table 2) of the thin sections of Norton County and Cumberland Falls in this study and Watters and Prinz (1979), the 3D results show higher abundances of metal and sulfides (e.g., in Cumberland Falls, 5.4 vol.% metal and sulfides in 3D vs. 2D estimates of 1.8 vol.% in Watters and Prinz (1979) and 2 vol.% in this study; see supplementary data). Mount Egerton shows greater abundances of metal in 3D compared to 2D results in this study (2.5 vol.% vs. trace modal abundances; see supplementary

data), and a network of fractures and vugs are observed oriented preferentially along their long axes (Figure 5). Peña Blanca Spring exhibits similar mineral abundances in both 2D and 3D. The 3D modal abundance estimates for Shallowater exhibit higher abundances of weathering products (9.7 vol.% vs. trace modal abundances), similar abundances of metal (1.9 vol.% in each), and lower abundances of sulfides (1.1 vol.% vs. 3.5 vol.%) compared to 2D thin section estimates. On the basis of the comparison of areas and volumes between thin sections and XCT analyses (Table 1), respectively, the 3D sample volumes are orders of magnitude greater than the 2D thin section analyses.

Major-element mineral compositions

The average mineral compositions of the newer/lesser-studied aubrites are represented in Tables 4–8. The average mineral compositions of the well-studied aubrites are represented in Supplementary Material Tables S3–S7.

Pyroxenes – *Enstatite* – The dominant silicate phase in the studied meteorites is FeO-poor enstatite (Table 4), with the exception of one thin section of Norton County (Norton County 983), which consists of one large oldhamite (50% vol.%) surrounded by forsterite. The average enstatite compositions range from $En_{98.2}Fs_{0.2}Wo_{1.6}$ (Bishopville) to $En_{99.7}Fs_{0.1}Wo_{0.2}$ (Shallowater). The pyroxene in ALH 84007 has the highest FeO contents at 0.23 wt.%. *Diopside* – Diopside is less common than enstatite with modal abundances of trace to 3 vol.% with average compositions ranging from $En_{54}Fs_{0}Wo_{46}$ (Bishopville) to $En_{59}Fs_{0}Wo_{41}$ (ALH 84007). Among the studied aubrites, diopside exhibits continuous zonation consistent with subsolidus exchange during cooling, and exsolution. Bishopville and Cumberland Falls contain zoned diopside, while Peña Blanca Spring, MIL 07008, and LAR 04316 exhibit orthopyroxene exsolution lamellae in diopside.

Plagioclase – The aubrites show variable plagioclase compositions (Table 5), ranging from $Ab_{83}An_{15.3}Or_{1.7}$ in ALH 78113 to $Ab_{94.4}An_{2.1}Or_{3.5}$ in LAR 04316. Shallowater was previously found to contain oligoclase (Keil, 1968), but this was not observed in our thin sections. While most of the samples contain solely albite, Bishopville contains trace orthoclase ($Ab_{10.9}An_{0.2}Or_{88.9}$). Normal zoning in albite is found in Cumberland Falls, Khor Temiki, and Norton County. The other samples present homogeneous albite compositions.

Olivine – The aubrites contain nearly endmember forsterite ($Fo_{99.7–100}$) (Table 6). Cumberland Falls and Shallowater have the highest FeO contents in forsterite, with averages of 0.13 and 0.20 wt.%, respectively.

Fe, Ni Metal – The aubrites contain low-Ni kamacite (Table 7), spanning 1.5 wt.% Ni in MIL 13004 to 11.8 wt.% Ni in Shallowater. MIL 13004 and Shallowater show the most variable Ni contents in kamacite.

Sulfides – The sulfide compositions are presented in Table 8. *Troilite* **–** Troilite is observed in all studied meteorites and contains measurable Ti and Cr concentrations (>0.1 wt.% and >0.3 wt.%, respectively). Several troilite grains in Khor Temiki show the highest contents of Ti in troilite, referred to as titanoan troilite, with 8.4 wt.% Ti. *Daubréelite* **–** Zinc and Mn concentrations vary among the aubrites (a minimum of 0.12 wt.% Zn in Norton County and a maximum of 0.53 wt.% Zn in Khor Temiki, and a maximum of 1.8 wt.% Mn in Peña Blanca Spring). The Zn and Mn concentrations of ALH 84007 are 0.16 wt.% and 1.74 wt.%, respectively. *Alabandite* **–** Trace to minor amounts of alabandite were observed in the aubrites (Table 8). It occurs in association with troilite and measures up to 100 μm. *Oldhamite* **–** Oldhamite was observed in Bishopville,

Norton County, Peña Blanca Spring, and MIL 13004 (Table 8 and Table S7). The phase was found in association with other sulfides, such as troilite, daubréelite, and djerfisherite, and measured up to 6 mm (observed in Norton County 983; Wheelock et al., 1994). Concentrations of the cations in oldhamite grains range 53.7 to 55.8 wt.% Ca, 0.76 to 1.4 wt.% Mn, 0.04 to 0.48 wt.% Mg, and 0.03 to 0.4 wt.% Fe. *Djerfisherite* **–** Djerfisherite was only observed in ALH 84007, Bishopville and Peña Blanca Spring. Bishopville contains 0.01 wt.% Cl, whereas Peña Blanca Spring contains 1.3 wt.% Cl and ALH 84007 contains 1.4 wt.% Cl. Bishopville contains more Na (0.31 wt.%) than ALH 84007 (0.13 wt.% Na) and Peña Blanca Spring (0.08 wt.% Na). Bishopville's djerfisherite contains 1.9 wt.% Ni and 0.41 wt.% Cu, Peña Blanca Spring's djerfisherite contains 3.3 wt.% Ni and 1.25 wt.% Cu, and djerfisherite in ALH 84007 contains 0.34 wt.% Ni and 1.85 wt.% Cu. *Heideite* **–** Heideite was only observed in MIL 13004. It contains 0.04–0.13 wt.% Mn, and 1.23–1.37 wt.% Cr.

Phosphides – *Schreibersite*– Schreibersite was observed in five of the studied aubrites (ALH 78113, ALH 84007, Cumberland Falls, Norton County, and Shallowater), usually present as exsolution within metal, or in contact with metal grains. Cumberland Falls and Norton County contain much higher concentrations of Ni (42.9 wt.% and 40.4 wt.%, respectively) and much lower concentrations of Fe (42.1 wt.% and 44.0 wt.%, respectively) compared to Shallowater (9.9 wt.% Ni and 73.9 wt.% Fe). *Perryite* [$(Ni,Fe)_5(Si,P)_2$]**–** Perryite was only observed within a metal grain in Mount Egerton. The perryite grain contains variable Fe (10.9–12.4 wt.%) concentrations and restricted ranges in Si (11.6 to 11.8 wt.%) and P (4.0 to 4.2 wt.%) contents.

Bulk-rock trace element abundances

The heterogeneous nature of the aubrites is reflected in their bulk element patterns (Casanova et al., 1993; Keil 2010). Barrat et al. (2016) reported ICP-MS results of a comprehensive suite of aubrites. Here we show the results of ICP-MS dissolution as bulk rock compositions of ten aubrites (Table 9 and Figure 6). The data were normalized to CI (Ivuna-type carbonaceous) chondrites (McDonough and Sun, 1995). Mount Egerton is enriched in light rare earth elements (LREE) [$(La/Lu)_{CI}$ of 4.2] and shows a slightly positive Eu anomaly (Eu/Eu* = 1.1, with Eu* = $(Sm \times Gd)^{1/2}$). Bishopville and MIL 13004 are slightly depleted in LREE [$(La/Lu)_{CI}$ of 0.9 and 0.7, respectively]. Bishopville shows a large, positive Eu anomaly (Eu/Eu* = 1.6), and MIL 13004 has a slightly negative Eu anomaly (Eu/Eu* = 0.8). The large, positive Eu anomaly is expected in Bishopville, as this aubrite contains the greatest percentage of plagioclase by volume (Table 2) (Watters and Prinz, 1979; Barrat et al., 2016).

Bulk-rock oxygen isotopic compositions

The oxygen isotopic compositions ($\delta^{18}O$ and $\delta^{17}O$) of the aubrites are listed in Table 10. The compositions are heterogeneous among the meteorites, and the O three-isotope plot (Fig. 7) shows that the aubrites fall slightly below the Terrestrial Fractionation Line (TFL) (with the exception of Norton County and ALH 78113, which nearly falls on the TFL) with $\Delta^{17}O$ ranging from –0.014 to –0.051 (Table 10). The $\Delta^{17}O$ of several of the aubrites (ALH 78113, MIL 13004, Mount Egerton, and Norton County) plot lower on the TFL than the enstatite chondrite impact melts (Fig. 7) from Udry et al. (2019). Our results show a broad range of linearized $\Delta^{17}O$ values (a range of 0.014± 0.007 to 0.051 ± 0.023, and an average of 0.039 ± 0.018%) (Table 10). The O isotopic compositions of the aubrites are within error of previously published studies (Clayton and Mayeda, 1994; Miura et al., 2007; Barrat et al., 2016), but those authors recovered a narrower

range of linearized $\Delta^{17}O$ values (an average of 0.009 ± 0.010%). Unlike the Barrat et al. (2016) study, our sample of Bishopville does not show the heaviest $\delta^{18}O$ value, which was previously attributed to its high plagioclase content. Norton County and Peña Blanca Spring exhibit heavier $\delta^{18}O$ values. The aubrites in this study overlap the previous O isotope fields from Clayton and Mayeda (1994) and Barrat et al. (2016) and extend to heavier O isotope values (Fig. 7). In particular, LAR 04316, ALH 84007, MIL 13004, and MIL 07008 present heavier oxygen isotopic values than other aubrites.

^{39}Ar-^{40}Ar

The Bishopville sample analyzed at Rutgers University produced a disturbed-release spectra with a plateau age of 4297 ± 15 Ma (MSWD = 2.3; Figure 8), with six of 11-steps forming the plateau comprising ~83% of the total ^{39}Ar ($_K$)with an integrated Ca/K of 1.6624 ± 0.0021. The old age of the first low temperature step (Step-A, ~12% of the total ^{39}ArK) is likely due to a small amount of atmospheric Ar and some recoil loss and/or redistribution of $^{39}Ar_K$ (Note: this can be inferred from an $^{36}Ar/^{37}Ar_{Ca}$ $^{38}Ar/^{36}Ar$ isotope correlation diagram). The young age of the last four steps (the last 5% of the total $^{39}Ar_K$ released) indicate recoil of $^{39}Ar_K$ into the high-Ca phases/sites. When cast on an isotope correlation diagram, the isotope data define an isochron age of 4349 ± 64 Ma and a $^{40}Ar/^{36}Ar_{initial}$ that is indistinguishable from the nebular value (Figure 8a). The total fusion, plateau, and isochron ages are analytically indistinguishable at the alpha-95 percent confidence level. The best age estimate for the Rutgers analysis of Bishopville is the plateau age, 4284 ± 14 Ma. Further step-heating analyses conducted at Arizona State University on three fragments of a separate Bishopville subsample are generally in agreement with these results, with ages of 4219 ± 26 Ma and 4338 ± 8, 4246 ± 10 (Figures 8b-8d), accounting for 53%, 71% and 71% of the $^{39}Ar_K$ release, respectively.

DISCUSSION

Classification of newly described samples

The previously undescribed samples classified as aubrites (i.e., LAP 02233, MIL 07008, MIL 13004, and NWA 8396) are mineralogically and petrologically similar to aubrites (e.g., Keil, 2010 and references therein), with the exception of NWA 8396, which has affinities of impact-melted enstatite chondrites (see below). LAP 02233, MIL 07008, and MIL 13004 display modal abundances characteristic of aubrites (87 – 99 vol.% of enstatite and 0.1 – 2.3 vol.% of total sulfides) (Table 2). These samples also contain forsterite and diopside, which are phases commonly found in samples of aubritic, rather than enstatite chondritic, affinity (i.e., Okada et al., 1988; Keil, 1989; McCoy et al., 2018). The studied samples contain low abundances of metal, which is also characteristic of the aubrites, as formation on a differentiated parent body would segregate metal from silicates (e.g., Udry et al., 2019). Aubritic metal contains lower Si contents compared to enstatite chondrite meteorites (0.9 wt.% Si on average in aubrites versus 4 wt.% in enstatite chondrites; Watters and Prinz, 1979; Udry et al., 2019) and the studied samples contain 0.1 to 1 wt.% Si within metal (Table 7). Moreover, aubrites typically contain Ti-enriched troilite (up to 5.7 wt.% Ti; Watters and Prinz, 1979; Brett and Keil, 1986) compared to troilite measured in enstatite chondrites (0.27 to 0.77 wt.% Ti; Keil, 1968), and we find titanoan troilite within these samples (up to 4.7 wt.% Ti in MIL 07008; Table 8). Consequently, we verify that LAP 02233, MIL 07008, and MIL 13004 are all aubrites.

Relationship of Northwest Africa 8396 to the enstatite-rich chondrites

On the basis of textural, mineralogical and geochemical data, NWA 8396 is an impact melt rock from an enstatite chondrite parent body. This sample contains unfractionated modal abundances of plagioclase (8 vol.%), troilite (3.6 vol.%), and metal (trace) similar to other enstatite chondrites (Van Niekerk et al., 2014; Udry et al., 2019). Additionally, two grains of K-feldspar were observed during its initial classification (Meteoritical Bulletin and Carl Agee, personal communication), and potassium feldspar is not typically found in the main group aubrites (the main group aubrites are: Aubres, Bishopville, Cumberland Falls, Khor Temiki, LAP 03719, LAR 04316, Mayo Belwa, Norton County, Peña Blanca Spring, and Pesyanoe). Potassium feldspar has been documented in the anomalous Mount Egerton and LEW 88055 samples, and it is also common in enstatite chondrites (Casanova et al., 1993). Unlike the coarse-grained pyroxenitic aubrites, NWA 8396 contains fine, rounded enstatite grains that are surrounded by Fe-rich weathering products, similar to other enstatite chondrite impact melt samples (e.g., Lin and Kimura, 1998; Rubin and Scott, 1997; Udry et al., 2019). The aubrites typically contain forsterite and diopside, while enstatite chondrites do not contain diopside. NWA 8396 does not contain forsterite or diopside; however, the absence of forsterite and diopside may be due to thin section sampling and is not strong evidence on its own for an enstatite chondrite parentage.

NWA 8396 is likely an impact melted enstatite chondrite because the sample shows enstatite surrounded by metal, and enstatite as inclusions within metal and troilite, which suggests complete melting as seen in Northwest Africa 7214 (Udry et al., 2019), and the fine-grained, equigranular enstatite suggests the sample cooled rapidly after an impact event (see NWA 4799 in Udry et al., 2019). Given that our analyses indicate this sample is an impact melted enstatite chondrite, it has been excluded from the remainder of the discussion that focuses solely on aubrites.

Insights into the origin and evolution of the aubrites

Cooling histories

The aubrites experienced radiogenic internal heating of their parent bodies that allowed for igneous differentiation to occur (e.g., Keil, 2010). The aubrites were likely derived from an enstatite chondrite-like precursor material, but not from the known enstatite-chondrite parent bodies due to mineralogical differences observed among the known aubrite and enstatite chondrite samples that cannot be reconciled by igneous differentiation (McCoy and Bullock, 2017; Udry et al., 2019). The aubrite parent bodies likely underwent violent collisional histories, explaining why most of the samples are brecciated (Keil, 2010). The lack of elemental zoning within the sulfide minerals indicates slower cooling rates. Normal zoning was observed within diopside in Cumberland Falls, and normal plagioclase zoning was observed in Norton County and Khor Temiki. Exsolution is prevalent among the aubrite samples: Plagioclase and diopside in Norton County exhibit exsolution lamellae, and an entire thin section of Norton County (967) appears as oriented clinopyroxene exsolution within orthopyroxene (agreeing with an equilibrium exsolution temperature of 1000 ˚C at 1 atm; Okada et al., 1988). Peña Blanca Spring also contains ortho-clinopyroxene exsolution, and thin, arcuate-shaped exsolution in diopside. Khor Temiki contains exsolution bands in troilite that are more Cr-rich than the host troilite, and daubréelite exsolution from troilite is a common occurrence in the studied samples. Alabandite in Cumberland Falls and Mount Egerton contains more Fe-rich exsolution, which is most likely troilite. The exsolution features among minerals within these meteorites suggest they formed at relatively slow cooling

rates. Evidence of slow cooling suggests the aubrites are intrusive rocks that were emplaced beneath the surface of their parent bodies. In addition, the coarse-grain sizes of enstatite (up to 10 cm long enstatite grains in Peña Blanca Spring; Lonsdale, 1947) and some of the sulfides (5 mm long oldhamite observed in thin section in this study) indicate the aubrite samples cooled slowly from their parent melts as slow cooling rates are more favorable for crystallization of large enstatite crystals (1 to 10 K/Ma; see Lorentz et al, 2021, Okada et al., 1988, and Keil, 1968 for temperature sequences applicable to aubrite cooling timescales).

The elusive origin of the aubrite parent bodies

Previous studies have reported a limited range in $\Delta^{17}O$ values for the aubrites that plot near or on the TFL (Clayton and Mayeda, 1994; Miura et al., 2007; Barrat et al., 2016; Zhu et al., 2021), and such a limited range in $\Delta^{17}O$ values has typically been used to infer that a parent body may have experienced a magma ocean stage (Greenwood et al., 2005, 2014, 2017; Scott et al., 2009; Barrat et al., 2016). In contrast to previous studies, the oxygen isotope results in this study (Table 10) indicate a slightly broader range of $\Delta^{17}O$ values for the aubrites that plot below or on the TFL (Table 10; Fig. 7). Taken together, the full range of aubrite $\delta^{18}O$ values from our study and previous studies indicates more O-isotopic heterogeneity among the aubrites than previously reported. The $\delta^{17}O$ and $\delta^{18}O$ values extend the aubrite oxygen isotope field to heavier isotope-enriched values for the samples that have not previously been analyzed for their oxygen isotopes (ALH 84007, LAR 04316, MIL 07008, and MIL 13004). Additionally, aliquots of Peña Blanca Spring, Mount Egerton, and ALH 78113 also span more enriched oxygen isotopic compositions compared to previous work (i.e., Barrat et al., 2016). The aubrites analyzed in this study do not expand the $\Delta^{17}O$ field, as they fall within ranges previously determined by Clayton and Mayeda (1984) and Barrat et al. (2016). This heterogeneity may indicate that the main group aubrites (excluding anomalous samples, such as Mount Egerton and Larned) originated from more than one common aubrite parent body, contrasting with the finding by Barrat et al. (2016). Alternatively, the heterogeneity could indicate that the aubrite parent body is more geochemically heterogeneous than previously suggested, which implies that the body did not undergo a complete melting (i.e., a global magma ocean) event. The O isotope analyses are expected to show a certain level of heterogeneity, depending on the material present in the analyzed chips (Udry et al. 2019). The heterogeneities among aliquots of each sample might be due to the fact that aubrites are typically brecciated and have clasts with different mineral modal abundances (although mostly composed of enstatite, they also contain diopside, forsterite, plagioclase, and trace sulfides). ALH 78113 and Norton County show the greatest variation of $\Delta^{17}O$ in this study. Some of the heterogeneity could also arise from the presence of chondritic clasts in brecciated aubrites, as also observed by Clayton and Mayeda (1996).

It is widely accepted that aubrites are derived from an enstatite chondrite-like precursor, which experienced differentiation, cooling, and impact events on one or more parent bodies, creating the suite of non-brecciated and brecciated rocks that we see in our meteorite collection (Keil, 2010 and references therein). Keil (1989) suggested the aubrites are derived from at least two parent bodies, the main aubrite parent body, which includes all aubrites except Shallowater, and the Shallowater parent body (noting that many new aubrites were not recovered at the time of the Keil 1989 study). The Shallowater meteorite likely experienced a three-stage cooling history due to a low-velocity collisional event that incorporated fragments of enstatite chondrite-like composition on the main body of molten, pure enstatite composition (Keil 1989; Keil 2010). Barrat

et al. (2016) further suggests two distinct groups of aubrites based on lithophile trace element abundances: 1) the main group aubrites, and 2) Mount Egerton and Larned (the latter being an anomalous aubrite containing more metal and silica polymorph compared to other aubrites). The main group aubrites show a flat or slightly LREE depleted pattern, while Mount Egerton and Larned show distinct REE patterns (Barrat et al., 2016). The aubrites in this study show similar trends as the whole rock unleached REE data from Barrat et al. (2016). Barrat et al. (2016) report that the main group aubrites (which are: Aubres, Bishopville, Cumberland Falls, Khor Temiki, LAP 03719, LAR 04316, Mayo Belwa, Norton County, Peña Blanca Spring, and Pesyanoe) show flat or LREE depleted REE patterns, with variable Eu anomalies, whereas the anomalous Mount Egerton sample displays a distinct LREE pattern and a slightly negative Eu anomaly. Overall, the REE patterns from this study are more enriched compared to Barrat et al. (2016). This enrichment is especially prevalent in the Peña Blanca Spring and Bishopville data. This may be due to the amount of oldhamite that was dissolved in this study, which would increase the overall bulk REE abundances, as REE's partition strongly into the structure of oldhamite, which is the main carrier of REE in aubrites (Floss et al., 1993; Wheelock et al. 1994).

Mount Egerton's voids and petrogenesis

Mount Egerton, deemed an anomalous metal-rich aubrite, has previously been suggested to represent the core-mantle boundary of its parent body and thereby a vital part of the differentiation sequence (Watters and Prinz, 1979). However, it has recently been suggested that Mount Egerton is derived from a distinct parent body due to its pyroxene LREE enrichments and siderophile trace element compositions in metal (Barrat et al., 2016). Mount Egerton is composed of enstatite and trace (this study) to 21 vol.% metallic Fe,Ni (Clevery et al., 1968), with trace abundances of troilite, perryite, and numerous weathered sulfide phases. To date, the mineralogy and structures of Mount Egerton have only been studied in 2D. We present a 3-dimensional rendering of Mount Egerton and show voids that are oriented along their long axes (see video in supplementary material and Figure 5). Oriented vesicles have been observed in other meteorites: Benedix et al. (2008) studied the L7 ordinary chondrite Patuxent Range (PAT) 91501 and interpreted the vesicles of similar orientation along long axes as neutrally buoyant vesicles to which metal and sulfide grains adhered. These vesicles may have been formed by gases that were freed during silicate partial melting (McCoy et al., 2006; Benedix et al., 2008). This mechanism is unlikely to be the case for Mount Egerton's oriented voids, as the voids are not spherical like the trapped gases inferred for PAT 91501, nor in close proximity to sulfide phases.

Large enstatites in enstatite chondrites exhibiting a grainy structure containing tubular voids have been observed (Olsen et al., 1977), and this growth phenomenon is a possible origin for the Mount Egerton enstatite. The melt from which Mount Egerton crystallized likely had an almost completely enstatitic composition; therefore, it may be possible to grow the coarse-grained enstatite slowly upon cooling. This slow growth rate could potentially produce different crystallographic orientations with the void defects. Moreover, Lorentz et al. (2020) observed voids of 500 μm diameters within enstatite in Pesyanoe and interpreted this to indicate that some of the Pesyanoe rocks crystallized under low lithostatic pressure. It is possible that Mount Egerton could also have crystallized under low lithostatic pressure, which would be at odds with it being from the core-mantle boundary of its parent body, unless it is sourced from its own, smaller, parent body rather than the core-mantle boundary of the aubrite parent body. Alternatively, since Mount Egerton is a find and is quite weathered, the voids may be a product of weathering at the Earth's

surface. Future electron backscatter diffraction (EBSD) analyses could clarify the origin of the enstatite voids present in the sample.

Brecciation/crystallization ages of Bishopville

According to the new Ar isotope data, the best minimum age estimates for Bishopville are the rather consistent plateau ages of 4219 ± 26, 4246 ± 10, 4297 ± 15, and 4338 ± 8 Ma (Figure 8). These ages are older than determined by a previous Ar-Ar study suggesting an age <4.1 Ga Bogard et al. (2010). The new ages are also older than ages of 3.5–3.9 Ga suggested by disturbed Rb-Sr isochrons (Compston et al., 1965; Minster et al., 1979). We interpret our new data as reflecting the timing of impact disturbance, but cannot rule out the possibility that they instead represent crystallization ages of individual clasts.

The new minimum ages are similar to impact ages (4.2 Ga) found for the newly reclassified enstatite chondrite impact melt sample NWA 4799 (Udry et al., 2019). Similar to the interpretation in Udry et al. (2019), the young impact age in Bishopville suggests its parent body was subjected to younger impact events than were previously established for the aubrite parent body (4.34 Ga; McCoy et al., 1995). Bishopville's plateau ages suggest that it is indeed an aubrite, and not of mercurian origin. Bishopville appears to be one of the most analogous enstatite-rich meteorite samples in our collection to that of a hypothetical mercurian sample (i.e., from a differentiated parent body, low bulk-FeO composition, exotic sulfides, albitic plagioclase compositions, and high plagioclase volume percentages; e.g. Watters and Prinz, 1979; van Acken et al., 2012), but the sample is likely too old to have originated from Mercury. According to crater statistics and impact flux models, mercurian rocks originating from the present-day surface are likely younger than 4.1 Ga due to resurfacing (Marchi et al., 2013). Additional isotopic analyses, such as Si-isotopes, may help to place better constraints on the origin of Bishopville.

Constraints on elemental partitioning within reduced planetary bodies

Enstatite-rich meteorites, such as aubrites and enstatite chondrites, originate from highly reduced parent bodies with fO_2 estimates ranging from 2 to 6 log units below the IW buffer (e.g., Keil 1968, 2010). They also represent the only samples of highly reduced materials from differentiated extraterrestrial parent bodies and hence, they are the only means to gain insights into the geochemical behavior of elements under highly reducing conditions from naturally-formed materials. This is particularly important for the burgeoning field of mercurian (also called hermian) geochemistry because Mercury also formed under highly reducing conditions with fO_2 estimates ranging from about 3 to 7 log units below the IW buffer (e.g., McCubbin et al., 2012; Zolotov et al., 2013; McCubbin et al., 2017). The composition of Mercury was poorly constrained prior to the MESSENGER mission, which orbited a spacecraft around Mercury from 2011 to 2015. The spacecraft had an X-Ray Spectrometer and a Gamma Ray and Neutron Spectrometer, which measured key rock-forming elemental abundances on the surface of the planet (e.g., Solomon et al., 2001; Nittler et al., 2011; Evans et al., 2012; Peplowski et al., 2015; Evans et al., 2015). MESSENGER data indicate that the planet has low Fe (<2 wt.%) and high S (up to 4 wt.%) abundances, as well as graphitic carbon in its crust (Nittler et al., 2011; Evans et al., 2012; Weider et al., 2012; Murchie et al., 2015; Peplowski et al., 2015; Vander Kaaden and McCubbin, 2015). From this information, it was determined that Mercury formed under highly reduced conditions, similar to that experienced by the aubrite parent bodies (e.g., Burbine et al., 2012, McCubbin et al., 2012; Zolotov et al., 2013).

631 The lack of identified samples from Mercury within the global meteorite collection means
632 that highly reduced meteorites may provide the best analogue for understanding the elemental
633 distributions within Mercury during its thermochemical evolution. The aubrite meteorites
634 represent valuable, natural, mercurian analogues (McCoy and Bullock, 2017). These meteorites
635 are similar to the mercurian surface in that they contain low Fe and high S abundances, and a low
636 bulk FeO composition (less than 1 wt.%, normative without metal components from McCubbin et
637 al., 2017). The aubrites contain enstatite, albitic plagioclase, Si-bearing metal and exotic sulfides,
638 such as FeS, MgS, CaS, which are inferred to be present on Mercury (e.g., Namur and Charlier,
639 2017; Vander Kaaden et al., 2017; McCoy et al., 2018). Although the aubrites are not perfect
640 petrological analogues to the mercurian surface and interior, along with the enstatite chondrite
641 impact melts (Udry et al., 2019), they represent the best analogue samples we have in current
642 collections. Mercury is a differentiated planet with likely more than nine different geochemical
643 regions on its surface that indicate the presence of diverse reservoirs within its interior (Nittler et
644 al., 2011; Peplowski et al., 2011; Weider et al., 2012; Charlier et al., 2013; Weider et al., 2015;
645 Lawrence et al., 2017; Vander Kaaden et al., 2017; Peplowski et al., 2019). Although aubrites are
646 differentiated and contain similar mineralogical phases as Mercury, their modal abundances are
647 different (McCubbin et al., 2017). For example, plagioclase on Mercury is likely double (up to
648 30%) the amount found in the most plagioclase-rich aubrite (i.e., Bishopville).
649 The reduced nature of the aubrite parent bodies and Mercury has raised many questions
650 regarding the geochemical behavior of typically lithophile elements in magmas at low fO_2.
651 Interpretations of magmatic processes on reduced rocky bodies are difficult at present because the
652 number of experimental studies relevant to the extremely low fO_2 and/or high sulfur content of the
653 aubrite parent bodies and Mercury are limited (e.g., Dickinson and McCoy, 1997; McCoy et al.,
654 1999; Malavergne et al., 2004; Malavergne et al., 2007; Rose-Weston et al., 2009; Ricolleau et al.,
655 2011; Chabot et al., 2014; Malavergne et al., 2014; Namur et al., 2016a; Vander Kaaden and
656 McCubbin, 2016; Vogel et al., 2018; Boujibar et al., 2019; Vander Kaaden et al., 2020; Anzures
657 et al., 2020; Steenstra et al., 2020a, 2020b, 2020c; Mouser et al., 2021), and our only natural
658 examples of what to expect with respect to element behavior in such oxygen-starved systems are
659 found in the highly reduced enstatite chondrites and aubrites (Keil 2010; Burbine et al., 2012; Udry
660 et al. 2019; Ingrao et al., 2019). At such reduced conditions, elements will deviate from their
661 typical geochemical behavior displayed at higher fO_2, which will impact the thermochemical
662 evolution of that body (e.g., McCoy et al., 1999; McCubbin et al., 2012; Cartier et al., 2014;
663 Kaufman, 2016; Vander Kaaden and McCubbin, 2016). For example, lithophile elements, such as
664 Mg and Ca, display chalcophile behavior in some highly reduced chondrites and achondrites
665 forming the minerals oldhamite and niningerite (McCoy et al., 1999), and Si and P display
666 siderophile behavior with elevated abundances in Fe-rich metals in those same meteorites (e.g.,
667 Ringwood, 1961; Berthet et al., 2009; Keil, 2010; Malavergne et al., 2010; McCoy et al., 2016;
668 Namur et al., 2016b). The systematic mineralogical analysis of aubrites conducted in this study
669 can help better define the elemental behavior at low fO_2 on Mercury.
670 We determined partitioning relationships of elements between bulk silicate, sulfide, and
671 metal phases within selected aubrites, and compare the results to partition coefficients determined
672 from petrologic experiments run under mercurian conditions corresponding to compositions of the
673 *Borealis Planitia* region of Mercury (Vander Kaaden and McCubbin, 2016). We include five
674 aubrites (Mount Egerton, LAP 02233, Shallowater, Bishopville, and Peña Blanca Spring) in these
675 calculations. These samples were selected based on their textures (non-brecciated samples being

the most ideal) and mineralogy (mineral diversity being preferable). Mount Egerton, LAP 02233, and Shallowater are non-brecciated and were used to calculate partition coefficients on the basis that they retain their intrinsic primary modal mineralogy due to a lack of brecciation. Bishopville contains djerfisherite and the highest content of silicate minerals by volume percentage. Furthermore, Bishopville has been identified as the most analogous sample to Mercury, although inferred not to be of mercurian origin. Peña Blanca Spring is one of the least brecciated samples and contains large, igneous enstatite grains, and djerfisherite. The partitioning behavior of elements within these aubrites act as a natural analogue to understand potential variations in the lithophile, siderophile, and chalcophile character of elements in reduced systems.

To compute the partition coefficients, we used the formula:

$$D_i^{X-Y} = c_i^X \div c_i^Y \quad (1)$$

where D_i^{X-Y} is the partition coefficient for element *i* between components *X* and *Y*, c_i^X is the concentration of element *i* in component *X* (i.e., bulk metal, bulk sulfide and/or bulk silicate) and c_i^Y is the concentration of element *i* in component *Y* (i.e., bulk metal, bulk sulfide and/or bulk silicate). The concentrations of each element within the bulk metal, bulk sulfide and/or bulk silicate were computed according to:

$$c_i^X\ (wt\%) = \left(\sum_{A=Phase\ X_1}^{All\ X\ phases} c_i^A \times M_{mass}^A \right) \div M_{mass}^X \quad (2)$$

where $c_i^X\ (wt\%)$ is the concentration (wt%) of element i in component *X* (i.e., bulk silicate, bulk sulfide, and/or bulk metal portion of the meteorite), c_i^A is the concentration (wt%) of element i in phase A, M_{mass}^A is the modal mass fraction of phase A in the entire sample, and M_{mass}^X is the modal mass fraction of component *X* in the entire sample. It should be noted that the calculated modal mineralogy is influenced by the heterogeneity of samples, which therefore affects these calculations. Our calculated mineral modes agree with past studies, and we estimate a maximum error of 7.2% for all phases. The following parenthetical mineral groupings were used to define the bulk silicate component (pyroxene + olivine + feldspar + roedderite), the bulk sulfide component (troilite + daubréelite + oldhamite + djerfisherite + alabandite), and the bulk metal component (Fe, Ni metal + phosphides) for each element.

Importantly, the modal abundances yield data based on volume, but our partition coefficients are computed using a mass-based mode. Consequently, our volume-based modes are converted to mass-based modes using the following equation:

$$M_{mass}^A = M_{volume}^A \times \rho^A \div \left(\sum_{A=Phase\ 1}^{All\ phases} M_{volume}^A \times \rho^A \right) \quad (3)$$

where M_{mass}^A is the modal mass fraction of phase A in the entire sample, M_{volume}^A is the volume-based mode for phase A in the entire sample as computed from the modal abundance data, and ρ^A is the density of phase A.

We used the modal abundances described in Table 2 and electron microprobe mineral major element data from Tables 4–8 and Supplementary Material Tables S3–7 to calculate masses, concentrations, and partition coefficients. The averages of mineral elemental data for each sample were converted from oxide to elemental data in the case of silicates, and compositions of all phases were normalized to 100 wt.%. Modal abundances, which were previously normalized to 100 vol.% in Table 2, were normalized a second time when sulfide/silicate upper limits are included. For example, djerfisherite was measured in both Bishopville and Peña Blanca Spring. However, the djerfisherite volume percentage was essentially 0 vol.% of the thin section, thereby making the mineral's presence null in concentration calculations. Since djerfisherite is a crucial host of elements like K, Na, and Cl, it is important to use an upper limit of the possible djerfisherite mode for the calculations in samples containing this phase. We assume an upper limit of 0.1 vol.%. An upper limit of 0.1 vol.% was applied for perryite to account for this phosphide phase, for which one grain was observed in Mount Egerton. Although roedderite [$KNaMg_2(Mg_3Si_{12})O_{30}$] has been observed in Peña Blanca Spring (Kaufman et al., 2016), we did not find this mineral in our thin sections, but have included an upper limit of 0.1 vol.% of this mineral as well to account for the potential silicate diversity and hosts of K and Na observed in aubrites. The sulfide-silicate and metal-silicate partition coefficients for each element in each sample are plotted in Figure 9 and compared to the experimental data from Vander Kaaden and McCubbin (2016).

The bulk distribution plots for Peña Blanca Spring, Shallowater, Bishopville, Mount Egerton, and LAP 02233 (Fig. 9) show that Fe is most likely to behave as a siderophile element, or as a chalcophile element within error. Iron is unlikely to behave as a lithophile element in the aubrites. We observe that Si and Mg exhibit overwhelmingly lithophile behavior in the studied samples, and S always exhibits more chalcophilic affinity. Measurements of Cl were only above detection in djerfisherite from Peña Blanca Spring (Table S7). All other sulfides, metals, and silicates in the aubrites yielded Cl abundances below detection, indicating that Cl likely exhibits chalcophile behavior in aubrites; however, more detailed studies of Cl in aubrite phases at trace abundances are needed to quantify the distribution of Cl among sulfide, silicate, and metal phases. Similarly, only metals exhibited P abundances above detection in the aubrites, indicating that P exhibits siderophile behavior in the aubrites. More detailed studies of P in aubrite phases at trace abundances are needed to quantify the partitioning behavior of P between sulfide, silicate, and metal phases.

The range of elemental affinities and partitioning heterogeneity exhibited at reducing conditions among the aubrites is reflected in the data for Ca, Na, Ti, Cr, Mn, and K. Calcium is predominantly lithophile in Shallowater, Mount Egerton, and LAP 02233, but it exhibits predominantly chalcophile affinities in Peña Blanca Spring and Bishopville. This variation in Ca affinity is correlated to the modal abundance of oldhamite relative to Ca-bearing silicate phases like plagioclase and Ca-rich pyroxene. Likewise, Na is a chalcophile element within Peña Blanca Spring, Mount Egerton, and LAP 02233, but a lithophile element within Shallowater and Bishopville. The behavior of Na is highly sensitive to the modal abundance of albite. Titanium and chromium, observed in troilite and daubréelite, respectively, exhibit chalcophile tendencies in the studied samples. Manganese exhibits chalcophile behavior within the studied samples with the exception of LAP 02233, where it presents lithophile affinity. Potassium reflects a range of behavior, from chalcophilic within Peña Blanca Spring and LAP 02233, to lithophile in Shallowater.

A major finding from Vander Kaaden and McCubbin (2016) is that Ca and Mg would not become substantial components in sulfide phases on Mercury unless the abundances of Fe, Cr, Mn, and Ti were deficient relative to the available sulfide components in the mercurian system. Our observations differ in the aubrites, in that Ti, Cr, K, Na, and Cl can be substantial components in sulfides within aubrites if the system has a paucity of Fe, Ca, and Mn. Given this trend and the low Cr, Mn, and Ti abundances present on Mercury (Vander Kaaden et al., 2017), it is most likely that CaS and MgS would be the major sulfide phases present on the surface of Mercury. From our calculated partition coefficients, we find that Mn- and Ca-bearing sulfides are the predicted sulfide phases, followed by Cr-, Ti-, K-, Na-, and Cl-bearing sulfides. This is reflected in our petrographic observations of the aubrite samples, as alabandite occurs in assemblages with daubréelite, troilite, and oldhamite.

Most of the partition coefficients calculated from aubrite geochemical data in this study show similar characteristics as those calculated under mercurian conditions in Vander Kaaden and McCubbin (2016). However, K, Ca, Na, and Cl show greater lithophile behavior in Vander Kaaden and McCubbin (2016) than the chalcophile behavior predicted from our study. These discrepancies are likely due to differences in modal abundances and instrument sensitivity. The aubritic abundances of minor phases, such as exotic sulfides, may vary in the analyzed thin sections, which has been shown in Table 2. Larger variations in elements like Cr, S, K, Na, Ca, and Cl are to be expected if sampling affects these minor phases. The sampling effect is less apparent for elements found in major phases, such as Si, Mg, and Fe. The differences with Vander Kaaden and McCubbin (2016) may also be attributed to differences in composition between Mercury and the aubrites or differences in pressure, temperature, or fO_2 among the different bodies. For instance, Vander Kaaden and McCubbin (2016) ran experiments across the pressure range of the mercurian mantle (0.5 to 5 GPa), at very low oxygen fugacity (IW 0 to -7). Moreover, Steenstra et al. (2020c) investigated the distribution of volatiles during core formation in reduced bodies and experimentally determined that all volatile elements behave as chalcophile and potentially siderophile elements. Similar to their study, we find Ti, Cr, and Mn are more chalcophile than lithophile, but our results show Mg behaving as a lithophile element rather than chalcophile. Coupling the results of low fO_2 experimental data and geochemistry from natural samples lends useful information about the geochemistry and elemental behavior in reduced magmatic systems. Elemental behavior is clearly different under varying fO_2, signifying that reduced parent bodies, such as aubrite and enstatite chondrite parent bodies as well as Mercury, undergo thermochemical evolution pathways that are in stark contrast to more oxidized bodies like the Earth, Moon, and Mars.

Implications for the curation and processing of aubrites

XCT as an important reconnaissance tool in the curation and processing of aubrites

XCT has been utilized in the field of advanced curation to better characterize precious astromaterial samples and to make decisions about how and where to process samples (McCubbin et al., 2019). In this study, we show that X-ray computed tomography offers particularly useful benefit to the study of aubrites because of their coarse-grained nature. XCT offers the opportunity to study large, and hence more representative, amounts of sample material, as 3D analyses show more representative amounts of minor phases, including sulfides, metal, and weathering products, than in modal analyses conducted on 2D sections. The 3D analyses have implications for sample

preservation: rather than destroying precious meteoritic material for thin sections and analyzing the minerals present, XCT allows the user to select targeted areas of interest for future study in a non-destructive manner to make more informed 2D slices through the sample. XCT should be used as a reconnaissance tool for other coarse-grained and complex precious materials.

Terrestrial contamination of aubrites

Aubrites and other samples from highly reduced parent bodies have a highly reactive mineralogy that is incompatible with water and the O_2-rich atmosphere at the Earth's surface. Terrestrial alteration is pervasive in most aubrites, including some falls, with the sulfide and metal phases being the first to be affected by weathering (Van Niekerk et al., 2014; Udry et al., 2019). In particular, when oldhamite weathers, it often develops a lattice–appearance, which we observed in Bishopville. Sulfide weathering was also evident in sulfides analyzed in Mount Egerton, Cumberland Falls, and MIL 13004. Sulfides in these samples produce low totals when analyzed by EPMA, which may be attributed to S oxidizing to form sulphates (Rubin, 1997). Additionally, djerfisherite within Bishopville contains low Cl, which may indicate a decomposition product of the mineral. Within MIL 13004, a caswellsilverite ($NaCrS_2$) grain was altered to a Na-Cr-bearing sulfide (potentially schöllhornite) due to hydrous interactions (El Goresy et al., 1988). The bulk rock trace element data also shows evidence of terrestrial alteration based on elevated Ba and Sr abundances (e.g., 4.85 ppm Ba and 11.99 ppm Sr in Bishopville).

The incompatible nature of the metal and sulfide mineralogy in highly reduced meteorites and the conditions at the Earth's surface indicates that additional care should be taken to preserve highly reduced meteorites over long timescales. A similar topic was discussed recently in the context of Mercury sample return by Vander Kaaden et al (2019), where they outlined steps to preserve highly reactive metal and sulfide phases that might be present in returned samples from Mercury. Some of those same measures should be taken for aubrites, especially for any future aubrite falls. Most critical is to remove the sample from the Earth's atmosphere and hydrosphere by storing it under vacuum or within a dry, inert atmosphere.

SUMMARY

By conducting a systematic petrographic and geochemical study of a comprehensive subset of aubrites, we conclude that:

- According to petrologic evidence, aubrites underwent slow cooling as observed by the ubiquitous presence of mineral exsolution and large pyroxene crystal sizes. Their slow cooling history might indicate an intrusive crustal origin.
- X-ray computed tomography shows different modal mineralogical results compared to the more common 2D thin section approach, and Mount Egerton's voids within enstatite may provide insight into the anomalous rock's formation history.
- The aubrite parent bodies may be more heterogeneous than originally expected, based on O isotopic compositions. The meteorites may be derived from many parent bodies, or their parent body may not have experienced a complete melting (i.e., global magma ocean) event.
- The aliquots of the Bishopville aubrite show the rather consistent plateau ages of 4219 ± 26, 4246 ± 10, 4297 ± 15, and 4338 ± 8 Ma, likely representing disturbance ages related to impact.

- The partition coefficients computed in this study from non-brecciated, highly reduced aubrites are broadly similar to partition coefficients computed from experimental studies conducted under mercurian conditions. Additionally, Cr-, Mn-, and Ti-bearing sulfides are likely to be phases present in reduced planetary systems.

Acknowledgements – We thank Daniel Kent Ross for his help and advice with using the electron microprobe at NASA JSC, and for his mentorship to Z.E.W. to create sulfide analytical routines. Kent is dearly missed, and we dedicate this work to his memory. We thank Dr. Minghua Ren for his help with electron microprobe mapping. We thank Dr. Carl Agee for his helpful discussions about NWA 8396. We thank Dr. Shichun Huang for his help with ICP-MS analyses, and Dr. Simon Jowitt for helpful discussions about bulk rock data and detection limits. Dr. Matthew Colbert is thanked for assistance with XCT software. We thank the Associate Editor, Dr. Alex Ruzicka, and external reviewers Dr. Maud Boyet and Dr. Makoto Kimura for their helpful and insightful reviews of this work. This work was partially funded by the UNLV Faculty Opportunity Award to A.U. Support for this research was provided in part by NASA's planetary science research program.

865 REFERENCES

866

867 Anzures, B.A., Parman, S.W., Milliken, R.E., Namur, O., Cartier, C., Wang, S. 2020. Effect of
868 sulfur speciation on chemical and physical properties of very reduced mercurian melts.
869 *Geochimica et Cosmochimica Acta* 286: 1-18.
870 Berthet S., Malavergne V., and Righter K. 2009. Melting of the Indarch meteorite (EH4 chondrite)
871 at 1 GPa and variable oxygen fugacity: Implications for early planetary differentiation
872 processes. *Geochimica et Cosmochimica Acta* 73(20): 6402-6420.
873 Barrat J. A., Greenwood R. C., Keil K., Rouget M. L., Boesenberg J. S., Zanda B., and Franchi I.
874 A. 2016. The origin of aubrites: Evidence from lithophile trace element abundances and
875 oxygen isotope compositions. *Geochimica et Cosmochimica Acta* 192:29–48.
876 Berhet S., Malavergne V., Righter K. 2009. Melting of the Indarch meteorite (EH4 chondrite) at 1
877 GPa and variable oxygen fugacity: Implications for early planetary differentiation
878 processes. *Geochimica et Cosmochimica Acta* 73(20): 6402-6420.
879 Bogard, D. D., Dixon, E. T., and Garrison, D. H. 2010. Ar-Ar ages and thermal histories of enstatite
880 meteorites. *Meteroritics and Planetary Science* 45:723-742.
881 Bouhifd, M.A., Gautron, L., Bolfan-Casanova, N., Malavergne, V., Hammouda, T., Andrault, D.,
882 Jephcoat, A.P., 2007. Potassium partitioning into molten iron alloys at high-pressure:
883 Implications for Earth's core. *Physics of the Earth and Planetary Interiors* 160: 22-33.
884 Boujibar, A., Habermann, M., Righter, K., Ross, D.K., Pando, K., Righter, M., Chidester, B.A.,
885 Danielson, L.R., 2019. U, Th, and K partitioning between metal, silicate, and sulfide and
886 implications for Mercury's structure, volatile content, and radioactive heat production.
887 *American Mineralogist* 104: 1221-1237.
888 Brett R., and Keil K. 1986. Enstatite chondrites and enstatite achondrites (aubrites) were not
889 derived from the same parent body. *Earth and Planetary Science Letters* 81:1–6.
890 Brett R., and Sato M. 1984. Intrinsic oxygen fugacity measurements on seven chondrites, a
891 pallasite, and a tektite and the redox state of meteorite parent bodies. *Geochimica et*
892 *Cosmochimica Acta* 48, 111-120.
893 Burbine T. H., McCoy T. J., Nittler L. R., Benedix G. K., Cloutis E. A., and Dickinson T. L. 2012.
894 Spectra of extremely reduced assemblages: Implications for Mercury. *Meteoritics and*
895 *Planetary Science* 37:1233–1244.
896 Cartier C., Hammouda T., Doucelance R., Boyet M., Devidal J.-L and Moine B., 2014.
897 Experimental study of trace elements partitioning between enstatite and melt in Enstatite-
898 Chondrites at low oxygen fugacity and 5 GPa. *Geochim. Cosmochim. Acta*, 130, 167-187.
899 Casanova, I., Keil, K., and Newson, H. E. 1993. Composition of metal in aubrites: constraints on
900 core formation. *Geochimica et Cosmochimica Acta* 57: 675-682.
901 Castaing, R. 1951. Application of electron probes to local chemical and crystallographic
902 analysis. *Ph. D. Thesis (University of Paris)*.
903 Chabot N.L., and Drake M.J. 1999. Potassium solubility in metal: The effects of composition at
904 15 kbar and 1900˚C on partitioning between iron alloys and silicate melts. *Earth and*
905 *Planetary Science Letters* 172, 323-335.
906 Chabot, N.L., Wollack, E.A., Klima, R.L. and Minitti, M.E. 2014. Experimental constraints on
907 Mercury's core composition. *Earth and Planetary Science Letters* 390: 199-208.

908 Charlier B., Grove T. L., and Zuber M. T. 2013. Phase equilibria of ultramafic compositions on
909 Mercury and the origin of the compositional dichotomy. *Earth and Planetary Science*
910 *Letters* 363:50–60.
911 Clayton R. N., Mayeda T. K., and Rubin A. 1984. Oxygen isotopic composition of enstatite
912 chondrites and aubrites. *Journal of Geophysical Research* 89:C245–C249.
913 Clayton R. N., and Mayeda T. K. 1996. Oxygen isotope studies of achondrites. *Geochimica et*
914 *Cosmochimica Acta* 60:1999–2017.
915 Compston, W., Lovering, J. F. and Vernon, M. J. 1965. The rubidium-strontium age of the
916 Bishopville aubrite and its component enstatite and feldspar. *Geochimica et Cosmochimica*
917 *Acta* 29:1085-1099.
918 Dickinson, T.L. and McCoy, T.J. 1997. Experimental rare-earth-element partitioning in oldhamite:
919 Implications for the igneous origin of aubritic oldhamite. *Meteoritics and Planetary*
920 *Science* 32:395-412.
921 Ebel D.S. and Sack R. 2013. Djerfisherite: Nebular Source of Refractory Potassium. *Contributions*
922 *to Mineralogy and Petrology* 166: 924-934.
923 El Goresy A., Yabuki H., Ehlers K., Woolum D., and Pernicka E. 1988. Qingzhen and Yamato-
924 691: A tentative alphabet for the EH chondrites. *Proc. NIPR Symp. Antarct. Meteorites* 1:
925 65-101.
926 Evans L. G., Peplowski P. N., Rhodes E. A., Lawrence D. J., McCoy T. J., Nittler L. R., Solomon
927 S. C., Sprague A. L., Stockstill-Cahill K. R., Starr R. D., Weider S. Z., Boynton W. V.,
928 Hamara D. K., and Goldsten J. O. 2012. Major element abundances on the surface of
929 Mercury: Results from the MESSENGER Gamma-Ray Spectrometer. *Journal of*
930 *Geophysical Research: Planets* 117:117.
931 Evans L. G., P.N. Peplowski, F.M. McCubbin, T.J. McCoy, L.R. Nittler, M.Y. Zolotov, D.S. Ebel,
932 D.J., R.D. Starr, S.Z. Weider, S.C. Solomon. 2015. Chlorine on the surface of Mercury:
933 MESSENGER gamma-ray measurements and implications for the planet's formation and
934 evolution. *Icarus* 257:417–427.
935 Fegley, B. and Cameron, A.G.W. 1987. A vaporization model for iron/silicate fractionation in the
936 Mercury proto planet. *Earth and Planetary Science Letters* 82: 207-222.
937 Floss C., Strait M.M., Crozaz, G. 1990. Rare Earth elements and the petrogenesis of aubrites.
938 *Geochimica et Cosmochimica Acta* 54: 3553-3558.
939 Floss C., and Crozaz G. 1993. Heterogeneous REE patterns in oldhamite from aubrites: Their
940 nature and origin. *Geochimica et Cosmochimica Acta* 57:4039–4057.
941 Fogel R. A. 1997. On the significance of diopside and oldhamite in enstatite chondrites and
942 aubrites. *Meteoritics & Planetary Science* 591:577–591.
943 Fogel, R.A. 1998. High-Sulfur/Low-Iron Silicate Melts: Low-Oxygen-Fugacity Phenomena of
944 Importance to Aubrite Formation. Meteoritics and Planetary Science Supplement 33, A52.
953 Friedrich, J. M., Macke, R. J., Wignarajah, D. P., Rivers, M.L., Britt, D. T., and Ebel, D. S. 2008.
954 Pore Size Distribution in an Uncompacted Equilibrated Ordinary Chondrite. *Planetary and*
955 *Space Science* 56: 895–900
956 Friedrich J. M., Weisberg M. K., Malecek L. C., Nehru C. E. 2021. Three-dimensional petrography
957 of the Tucson meteorite. *Meteoritics & Planetary Science.* 56: 1933–1943.
958 Greenwood R.C., Franchi I.A., Jambon A., Buchanan P.C. 2005. Widespread magma oceans on
959 asteroidal bodies in the early solar system. *Nature* 435: 916-918. 43

960 Greenwood R.C., Burbine T.H., Miller M.F., Franchi I.A. 2017. Melting and differentiation on
961 early formed asteroids: The perspective from high precision oxygen isotopes. *Chemie der*
962 *Erde - Geochemistry* 77: 1-43.
963 Hanna R.D. and Ketcham R.A. 2017. 3D morphology of fine-grained rims in CM Murchison. 47th
964 Lunar and Planetary Science Conference, The Woodlands, Texas.
965 Huang S., and Frey F. A. 2003. Trace element abundances of Mauna Kea basalt from phase 2 of
966 the Hawaii Scientific Drilling Project: Petrogenetic implications of correlations with major
967 element content and isotopic ratios. *Geochemistry, Geophysics, Geosystems* 4: 8711.
968 Ingrao N.J., Hammouda T., Boyet M., Gaborieau M., Moine B., Vlastelic I., Bouhifd M.A.,
969 Devidal J.-L., Mathon O., Testemale D., Hazemann J.-L., Proux O., 2019. Rare Earth
970 Elements Partitioning Between Sulphides and Melt: Evidence for Yb^{2+} and Sm^{2+} in EH
971 Chondrites. *Geochimica and Cosmochimica Acta*, 265, 182-197.
972 Kaufman S.V., Corrigan C.M., McCoy T.J., Bullock E.S. 2016. Mineral associations in enstatite
973 chondrites: possible insights into minerals on Mercury. In *47th Lunar and Planetary*
974 *Science Conference*, abstract #2743.
975 Keil K. 1968. Mineralogical and chemical relationships among enstatite chondrites. *Journal of*
976 *Geophysical Research* 73:6945–6976.
977 Keil K. 1989. Enstatite meteorites and their parent bodies. *Meteoritics* 208:195–208.
978 Keil K., and Bischoff A. 2008. Northwest Africa 2526: A partial melt residue of enstatite chondrite
979 parentage. *Meteoritics and Planetary Science* 43:1233–1240.
980 Keil K. 2010. Enstatite achondrite meteorites (aubrites) and the histories of their asteroidal parent
981 bodies. *Chemie der Erde - Geochemistry* 70:295–317.
982 Kimura M., Lin Y.-T., Ikeda Y., El Goresy A., Yanai K., and Kojima H. 1993. Mineralogy of
983 Antarctic aubrites, Yamato-793592 and Allan Hills-78113: Comparison with non-
984 Antarctic aubrites and E-chondrites. *Proc. NIPR Symp. Antarc. Meteorites* 6: 186-
985 203.Larimer J.W., and Buseck P.R. 1974. Equilibrium temperatures in enstatite
986 chondrites. *Geochimica et Cosmochimica Acta* 38, 471-477.
987 Lawrence, D.J., Peplowski, P.N., Beck, A.W., Feldman, W.C., Frank, E.A., McCoy, T.J., Nittler,
988 L.R., Solomon, S.C., 2017. Compositional terranes on Mercury: Information from fast
989 neutrons. *Icarus* 281: 32-45.
990 Lin Y. and Kimura M. 1998. Petrographic and mineralogical study of new EH melt rocks and a
991 new enstatite chondrite grouplet. Meteoritics & Planetary Science 33: 501-511.
992 Lodders K., Palme H., Wlotzka F. 1993. Trace elements in mineral separates of the Pena Blanca
993 Spring aubrite: Implications for the evolution of the aubrite parent body. *Meteoritics* 28:
994 538-551.
995 Lodders, K. and Fegley Jr., B. 1998. *The Planetary Scientist's Companion*. Oxford: Oxford
996 University Press, New York.
997 Lonsdale, J.T. 1947. The Pena Blanca Spring Meteorite, Brewster County, Texas. *American*
998 *Mineralogist* 32: 354-364.
999 Lorenz, C.A., Ivanova, M.A., Brandstaetter, F., Kononkova, N.N., and Zinovieva, N.G. 2020.
1000 Aubrite Pesyanoe: Clues to composition and evolution of the enstatite achondrite parent
1001 body. *Meteoritics & Planetary Science* 55(12): 2670–2702.

1002 Maloy A. K., and Treiman A. H. 2007. Evaluation of image classification routines for determining
1003 modal mineralogy of rocks from X-ray maps. *American Mineralogist* 92:1781–1788.
1004 Malavergne V., Toplis M. J., Berthet S., and Jones J. 2010. Highly reducing conditions during
1005 core formation on Mercury: Implications for internal structure and the origin of a
1006 magnetic field. *Icarus* 206(1): 199-209.
1007 Malavergne, V., Cordier, P., Righter, K., Brunet, F., Zanda, B., Addad, A., Smith, T., Bureau, H.,
1008 Surblé, S., Raepsaet, C., Charon, E. and Hewins, R.H. 2014. How Mercury can be the most
1009 reduced terrestrial planet and still store iron in its mantle. *Earth and Planetary Science Letters*
1010 394: 186-197.
1011 Malavergne, V., Siebert, J., Guyot, F., Gautron, L., Combes, R., Hammouda, T., Borensztajn, S.,
1012 Frost, D. and Martinez, I. 2004. Si in the core? New high-pressure and high-temperature
1013 experimental data. *Geochimica Et Cosmochimica Acta* 68: 4201-4211.
1014 Malavergne, V., Tarrida, M., Combes, R., Bureau, H., Jones, J. and Schwandt, C. 2007. New high-
1015 pressure and high-temperature metal/silicate partitioning of U and Pb: Implications for the
1016 cores of the Earth and Mars. *Geochimica Et Cosmochimica Acta* 71: 2637-2655.
1017 Marchi, S., Chapman, C. R., Fassett, C. I., Head, J. W., Bottke, W. F., & Strom, R. G. 2013. Global
1018 resurfacing of Mercury 4.0–4.1 billion years ago by heavy bombardment and volcanism.
1019 *Nature* 499(7456): 59.
1020 McCoy T. J. Keil K., Bogard D.D., Garrison D.H., Casanova I., Lindstrom M.M., Brearly A.J.,
1021 Kehm K., Nichols R.H., Hohemberg C.M. 1995. Origin and history of impact-melt rocks
1022 of enstatite chondrite parentage. *Geochimica et Cosmochimica Acta* 59:161–175.
1023 McCoy T. J., Dickinson T. L., and Lofgren G. E. 1999. Partial melting of the Indarch (EH4)
1024 meteorite: A textural, chemical, and phase relations view of melting and melt migration.
1025 *Meteoritics and Planetary Science* 34:735–746.
1026 McCoy T. J., and Bullock E. S. 2017. Differentiation Under Highly Reducing Conditions: New
1027 Insights from Enstatite Meteorites and Mercury. *Planetesimals* 44: 71–91.
1028 McCoy T. J., Peplowski P. N., McCubbin F. M., and Weider S. Z. 2018. The Geochemical and
1029 Mineralogical Diversity of Mercury. In *Mercury: The View after MESSENGER*, edited by
1030 Solomon, S.C., Nittler, L.R., Anderson B. J. UK: Cambridge University Press. pp. 176–
1031 190.
1032 McCubbin F. M., Riner M. A., Vander Kaaden K. E., and Burkemper L. K. 2012. Is Mercury a
1033 volatile-rich planet? *Geophysical Research Letters* 39:1–5.
1034 McCubbin F. M., and McCoy T. J. 2016. Expected Geochemical and Mineralogical Properties of
1035 Meteorites from Mercury: Inferences from Messenger Data. 79th Annual Meeting of the
1036 Meteoritical Society.
1037 McCubbin F. M., Vander Kaaden K.E., Pelowski P.N., Bell A.S., Nittler L.R., Boyce J.W., Evans
1038 L.G., Keller L.P., Elardo S.M., McCoy T.J. 2017. A Low O/Si Ratio on the Surface of
1039 Mercury: Evidence for Silicon Smelting? *Journal of Geophysical Research: Planets*
1040 122:2053–2076.
1041 McCubbin, F.M., Herd, C.D.K., Yada, T., Hutzler, A., Allton, J.H., Calaway, M.J., Corrigan,
1042 C.M., Fries, M.D., Harrington, A.D., McCoy, T.J., Mitchell, J.L., Regberg, A.B., Righter,
1043 K., Snead, C.J., Tait, K.T., Zolensky, M., and Zeigler, R.A. 2019. Advanced Curation of
1044 Astromaterials for Planetary Science. *Space Science Reviews* 215, 1-48.

McCubbin, F.M., Lewis, J.A., Barnes, J.J., Elardo, S.M., and Boyce, J.W. 2021. The abundances of F, Cl, and H_2O in eucrites: Implications for the origin of volatile depletion in the asteroid 4 Vesta. *Geochimica et Cosmochimica Acta* 314, 270-293.

McDonough W.F. and Sun S. (1995) The composition of the Earth. *Chemical Geology*, 120, 223-253.

Merlet, C. 1994. An accurate computer correction program for quantitative electron probe microanalysis. *Microchimica Acta* 114(1): 363-376.

Minster, J.-F., Ricard, L.-P., and Allègre, C. J. 1979. ^{87}Rb-^{87}Sr Chronology of Enstatite Meteorites. *Earth and Planetary Science Letters* 44:420-440.

Miura Y. N., Hidaka H., Nishiizumi K., and Kusakabe M. 2007. Noble gas and oxygen isotope studies of aubrites: A clue to origin and histories. *Geochimica et Cosmochimica Acta* 71:251– 270.

Mouser, M.D., Dygert, N., Anzures, B.A., Grambling, N.L., Hrubiak, R., Kono, Y., Shen, G., Parman, S.W. 2021. Experimental Investigation of Mercury's Magma Ocean Viscosity: Implications for the Formation of Mercury's Cumulate Mantle, Its Subsequent Dynamic Evolution, and Crustal Petrogenesis. *Journal of Geophysical Research – Planets* 126: doi:10.1029/2021JE006946.

Murchie S. L., Klima R. L., Denevi B. W., Ernst C. M., Keller M. R., Domingue D. L., Blewett D. T., Chabot N. L., Hash C. D., Malaret E., Izenberg N. R., Vilas F., Nittler L. R., Gillis-Davis J. J., Head J. W., and Solomon S. C. 2015. Orbital multispectral mapping of Mercury with the MESSENGER Mercury Dual Imaging System: Evidence for the origins of plains units and low-reflectance material. *Icarus* 254: 287-305.

Namur O., Charlier B., Holtz F., Cartier C., and McCammon C. 2016a. Sulfur solubility in reduced mafic silicate melts: Implications for the speciation and distribution of sulfur on Mercury. *Earth and Planetary Science Letters* 448: 102-114.

Namur O., Collinet M., Charlier B., Grove T. L., Holtz F., and McCammon C. 2016b. Melting processes and mantle sources of lavas on Mercury. *Earth and Planetary Science Letters* 439: 117-128.

Namur O., and Charlier B. 2017. Silicate mineralogy at the surface of Mercury. *Nature Geoscience* 10:9–13.

Newton J., Franchi I. A., and Pillinger C. T. 2000. The oxygen-isotopic record in enstatite meteorites. *Meteoritics & Planetary Science* 35:689–698.

Nier A. O. 1950. A redetermination of the relative abundances of the isotopes of carbon, nitrogen, oxygen, argon, and potassium. *American Physical Society* 77, 789. https://link.aps.org/doi/10.1103/PhysRev.77.789

Nittler L. R., Starr R. D., Weider S. Z., McCoy T. J., Boynton W. V., Ebel D. S., Ernst C. M., Evans L. G., Goldsten J. O., Hamara D. K., Lawrence D. J., McNutt R. L., Schlemm C. E., Solomon S. C., and Sprague A. L. 2011. The Major-Element Composition of Mercury's Surface from MESSENGER X-ray Spectrometry. *Science* 333(6051): 1847-1850.

Okada A., Keil K., Taylor G. J., and Newsom H. 1988. Igneous history of the aubrite parent asteroid: Evidence from the Norton County enstatite achondrite. Meteoritics 23:59–74.

Pack, A., Tanaka R., Hering M., Sengupta S. 2016. The oxygen isotope composition of San Carlos olivine on the VSMOW2-SLAP2 scale. *Rapid Communications in Mass Spectrometry* https://doi.org/10.1002/rcm.7582.

1089 Olsen, E.J., Bunch, T., Jarosewich, E., Noonan, A.F. and Huss, G.I. 1977. Happy Canyon: A new
1090 type of enstatite achondrite. *Meteoritics* 12: 109-124. https://doi.org/10.1111/j.1945-
1091 5100.1977.tb00336.x
1092 Patzer A., Hill D. H., and Boynton W. V. 2001. Itqiy: A metal-rich enstatite meteorite with
1093 achondritic texture. *Meteoritics and Planetary Science* 36:1495–1505.
1094 Peplowski P. N. Evans L.G., Huack S.A., McCoy T.J. 2011. Radioactive elements on Mercury's
1095 surface from MESSENGER: implications for the planet's formation and evolution. *Science*
1096 333:1850-2.
1097 Peplowski, P.N., Stockstill-Cahill, K., 2019. Analytical Identification and Characterization of the
1098 Major Geochemical Terranes of Mercury's Northern Hemisphere. *Journal of Geophysical*
1099 *Research: Planets* 124: 2414-2429.
1100 Piatak N.M. 2012. Mineralogy and environmental geochemistry of historical iron slag, Hopewell
1101 Furnace National Historic Site, Pennsylvania, USA. *Applied Geochemistry*. 27: 623-643.
1102 Ricolleau, A., Fei, Y., Corgne, A., Siebert, J. and Badro, J. 2011. Oxygen and silicon contents of
1103 Earth's core from high pressure metal-silicate partitioning experiments. *Earth and Planetary*
1104 *Science Letters* 310: 409-421.
1105 Ringwood A.E. 1961. Silicon in the metal phase of enstatite chondrites and some geochemical
1106 implications. *Geochimica Et Cosmochimica Acta* 25:1-13.
1107 Rose-Weston, L., Brenan, J.M., Fei, Y.W., Secco, R.A. and Frost, D.J. (2009) Effect of pressure,
1108 temperature, and oxygen fugacity on the metal-silicate partitioning of Te, Se, and S:
1109 Implications for earth differentiation. *Geochimica Et Cosmochimica Acta* 73: 4598-4615.
1110 Rubin A.E. 1997. Mineralogy of meteorite groups. *Meteoritics and Planetary Science*. 32:231–
1111 247.
1112 Rubin A. E. and Scott E. R. D. 1997. Abee and related EH chondrite impact- melt breccias.
1113 Geochimica et Cosmochimica Acta 61: 425-435.
1114 Rubin, A. E. 2015. Shock and annealing in aubrites: Implications for parent body history.
1115 *Meteoritics & Planetary Science* 50 (7): 1217–1227.
1116 Ruzika A., Killgore M., Mittlefehldt D. W., Fries M.D. 2005. Portales Valley: Petrology of a
1117 metallic-melt meteorite breccia. *Meteoritics and Planetary Science* 40, 261-295.
1118 Scott E.D.R., Greenwood R.C., Franchi I.A., Sanders I.S. 2009. Oxygen isotopic constraints on
1119 the origin and parent bodies of eucrites, diogenites, and howardites. *Geochimica et*
1120 *Cosmochimica Acta* 73: 5835–5853
1121 Sharp Z. D. 1990. A laser-based microanalytical method for the in situ determination of oxygen
1122 isotope ratios of silicates and oxides. *Geochimica et Cosmochimica Acta* 54:1353–1357.
1123 Steenstra, E.S., Seegers, A.X., Putter, R., Berndt, J., Klemme, S., Matveev, S., Bullock, E.S., van
1124 Westrenen, W., 2020a. Metal-silicate partitioning systematics of siderophile elements at
1125 reducing conditions: A new experimental database. *Icarus* 335.
1126 Steenstra, E.S., Trautner, V.T., Berndt, J., Klemme, S., van Westrenen, W., 2020b. Trace
1127 element partitioning between sulfide-, metal- and silicate melts at highly reduced
1128 conditions: Insights into the distribution of volatile elements during core formation in
1129 reduced bodies. *Icarus* 335.
1130 Steenstra, E.S., van Westrenen, W. 2020c. Geochemical constraints on core-mantle
1131 differentiation in Mercury and the aubrite parent body. *Icarus* 340.

Steiger R. H. and Jager E. 1977. Subcommission on geochronology: Convention on the use of decay constants in geo- and cosmochronology. *Earth and Planetary Science Letters* 36, 359-362.

Tsuchiyama A., Uesugi K., Nakano T., Ikeda S. 2005. Quantitative evaluation of attenuation contrast of X-ray computed tomography images using monochromatized beams. *American Mineralogist* 90: 132-142.

Udry, A., Wilbur, Z.E., Rahib, R.R., McCubbin, F.M., Vander Kaaden, K.E., McCoy, T.J., Ziegler, K., Gross, J., DeFelice, C., Combs, L., Turrin, B.D., 2019. Reclassification of four aubrites as enstatite chondrite impact melts: potential geochemical analogues for Mercury. *Meteoritics and Planetary Scienc*e 54: 785–810

Vander Kaaden, K.E. and McCubbin, F.M. 2015. Exotic crust formation on Mercury: Consequences of a shallow, FeO-poor mantle. *Journal of Geophysical Research-Planets* 120, 195-209.

Vander Kaaden, K.E. and McCubbin, F.M. 2016. The origin of boninites on Mercury: An experimental study of the northern volcanic plains lavas. *Geochimica Et Cosmochimica Acta* 173, 246-263.

Vander Kaaden K. E., McCubbin F. M., Nittler L. R., Peplowski P. N., Weider S. Z., Frank E. A., and McCoy T. J. 2017. Geochemistry, mineralogy, and petrology of boninitic and komatiitic rocks on the mercurian surface: Insights into the mercurian mantle. *Icarus* 285:155–168.

Vander Kaaden, K.E., McCubbin, F.M., Byrne, P.K., Chabot, N.L., Ernst, C.M., Johnson, C.L., and Thompson, M.S. 2019. Revolutionizing Our Understanding of the Solar System via Sample Return from Mercury. *Space Science Reviews* 215, 1-30.

Vander Kaaden, K.E., McCubbin, F.M., Turner, A.A., Ross, D.K. 2020. Constraints on the Abundances of Carbon and Silicon in Mercury's Core from Experiments in the Fe-Si-C System. *Journal of Geophysical Research: Planets* 125(5).

Van Niekerk D., Keil K., and Humayun M. 2014. Petrogenesis of anomalous Queen Alexandra Range enstatite meteorites and their relation to enstatite chondrites, primitive enstatite achondrites, and aubrites. *Meteoritics and Planetary Science* 49:295–312.

Vogel, A.K., Jennings, E.S., Laurenz, V., Rubie, D.C. and Frost, D.J. 2018. The dependence of metal-silicate partitioning of moderately volatile elements on oxygen fugacity and Si contents of Fe metal: Implications for their valence states in silicate liquids. *Geochimica et Cosmochimica Acta* 237: 275-293.

Watters T. R., and Prinz M. 1979. Aubrites-Their origin and relationship to enstatite chondrites. In *Lunar and Planetary Science Conference Proceedings*. pp. 1073–1093.

Weider S. Z., Nittler L. R., Starr R. D., McCoy T. J., Stockstill-Cahill K. R., Byrne P. K., Denevi B. W., Head J. W., and Solomon S. C. 2012. Chemical heterogeneity on Mercury's surface revealed by the MESSENGER X-Ray Spectrometer. *Journal of Geophysical Research: Planets* 117:1–15.

Weider S. Z. Nittler L.R., Starr R.D., Crapster-Pregont E.J., Peplowski P.N. 2015. Evidence for geochemical terranes on Mercury: Global mapping of major elements with MESSENGER's X-Ray Spectrometer. *Earth and Planetary Science Letters* 416:109–120.

Weiler R. 2002. Cosmic-ray-produced noble gases in meteorites. *Reviews in Mineralogy and Geochemistry* 47 (1) 125-170.

1176 Weisberg M. K., Fogel R. A., and Prinz M. 1997. Kamacite-enstatite intergrowths in enstatite
1177 chondrites. In (abstract #1768). 28th Lunar and Planetary Science Conference. p. 523.
1178 Wheelock M.M., Keil K., Floss C., Taylor G.J., Crozaz G. 1994. REE geochemistry of oldhamite-
1179 dominated clasts from the Norton County aubrite: Igneous origin of oldhamite. *Geochimica*
1180 *et Cosmochimica Acta* 58: 449-458
1181 Zhang Y., Benoit, P.H., Sears D.W. 1995. The complex thermal history of the enstatite chondrites.
1182 *Journal of Geophysical Research: Planets* 100:9417-9438.
1183 Zolotov M. Y., Sprague A. L., Hauck S. A., Nittler L. R., Solomon S. C., and Weider S. Z. 2013.
1184 The redox state, FeO content, and origin of sulfur-rich magmas on Mercury. *Journal of*
1185 *Geophysical Research: Planets* 118:138–146.
1186

FIGURE CAPTIONS

Figure 1. Photomicrographs of the aubrites of focus in this study: a) Reflected light image (REF) of ALH 78113 showing schreibersite and kamacite. b) REF image of ALH 84007 sulfide assemblages containing daubréelite, troilite, and alabandite in contact with enstatite grains. c) Cross-polarized light (XPL) image of LAR 04316 showing enstatite and forsterite grains. d) XPL image of MIL 13004 depicting poikilitic forsterite grains within enstatite.

Figure 2. Back-scattered electron images of the aubrites of focus in this study: a) ALH 78113: sulfide assemblage present within metal. b) ALH 78113: daubréelite present within schreibersite exsolution in kamacite. c) ALH 84007: djerfisherite in contact with troilite. d) LAR 04316: sulfide assemblage with a weathered phase. e) MIL 07008: sulfide and metal assemblage. f) MIL 13004: alabandite and a Na-Cr-sulfide alteration phase, potentially schöllhornite. g) NWA 8396: anhedral daubréelite and troilite. h) NWA 8396: anhedral and weathered troilite and metal, and rounded enstatite.

Figure 3. Composite element maps of a) ALH 78113; b) ALH 84007; c) LAP 02233; d) LAR 04316; e) MIL 07008; f) MIL 13004; and g) NWA 8396. The overlays contain: Fe (red), Mg (green), and S (blue). Green = Enstatite; Dark red = Terrestrial alteration; Bright red = Fe,Ni metal; Black = Interstitial plagioclase; Light blue = daubréelite; Purple = troilite; and Dark blue = alabandite.

Figure 4. Impact melt observed within: a) and b) Bishopville; c) an enstatite grain in Cumberland Falls; and d) LAR 04316. The melt presents a schlieren pattern and contains Fe- and S-bearing spherules.

Figure 5. 2D Slice from the micro-XCT scan of Mount Egerton. Metal (yellow), sulfides (pink), vugs (turquoise), and larger vesicles (dark blue) are shown. This sample's texture is unique among the studied aubrites.

Figure 6. Bulk rock trace element patterns of the studied aubrites. Mount Egerton shows an anomalous REE pattern. The previously unstudied aubrites show similar REE patterns compared to the well-studied samples. Samples from Barrat et al. (2016) are plotted as dashed lines. The variable REE abundances and similar patterns for samples also analyzed by Barrat et al. (2016) could reflect REE-bearing mineral mode heterogeneity for phases such as oldhamite (i.e., the nugget effect), or potentially variation in REE abundances in REE-bearing phases and/or elemental redistribution as shown by Ruzicka et al. (2005).

Figure 7a. $\delta^{18}O$ versus $\delta^{17}O$ for the aubrite samples in this study, including the TFL and aubrite falls (blue envelope) and finds (pink envelope) from Barrat et al. (2016), data from Clayton and Mayeda (1984) in the green envelope, and data from Miura et al. (2007) in the purple envelope. Errors are smaller than the symbols. 7b) $\delta^{18}O$ versus $\Delta\ ^{17}O$ for the studied aubrites compared to the envelopes for EH and EL chondrites from Greenwood et al. (2017), in addition to the aubrite fields from past studies, listed above.

Figure 8. Ar^{39}-Ar^{40} step heating and isochron results for Bishopville analyses a) at Rutgers

University and b) - d) at Arizona State University. The pink shading indicates release intervals interpreted to represent age plateaus. The integrated ages were calculated from summed ^{39}Ar and ^{40}Ar release over the intervals interpreted to represent plateaus.

Figure 9. Elemental partitioning behavior of elements in Peña Blanca Spring, Shallowater, Bishopville, Mount Egerton, and LAP 02233 compared to petrologic experiments run under mercurian conditions from Vander Kaaden and McCubbin (2016). The partition coefficients computed in this study and plotted above are listed in Table 11. We observe heterogeneity in the elemental affinities of Ca, Na, Ti, Cr, Mn, and K, as their behavior is highly sensitive to the modal mineralogy.

(2016) in blue circles. The partition coefficients computed in this study and plotted above are in

Figure 1.

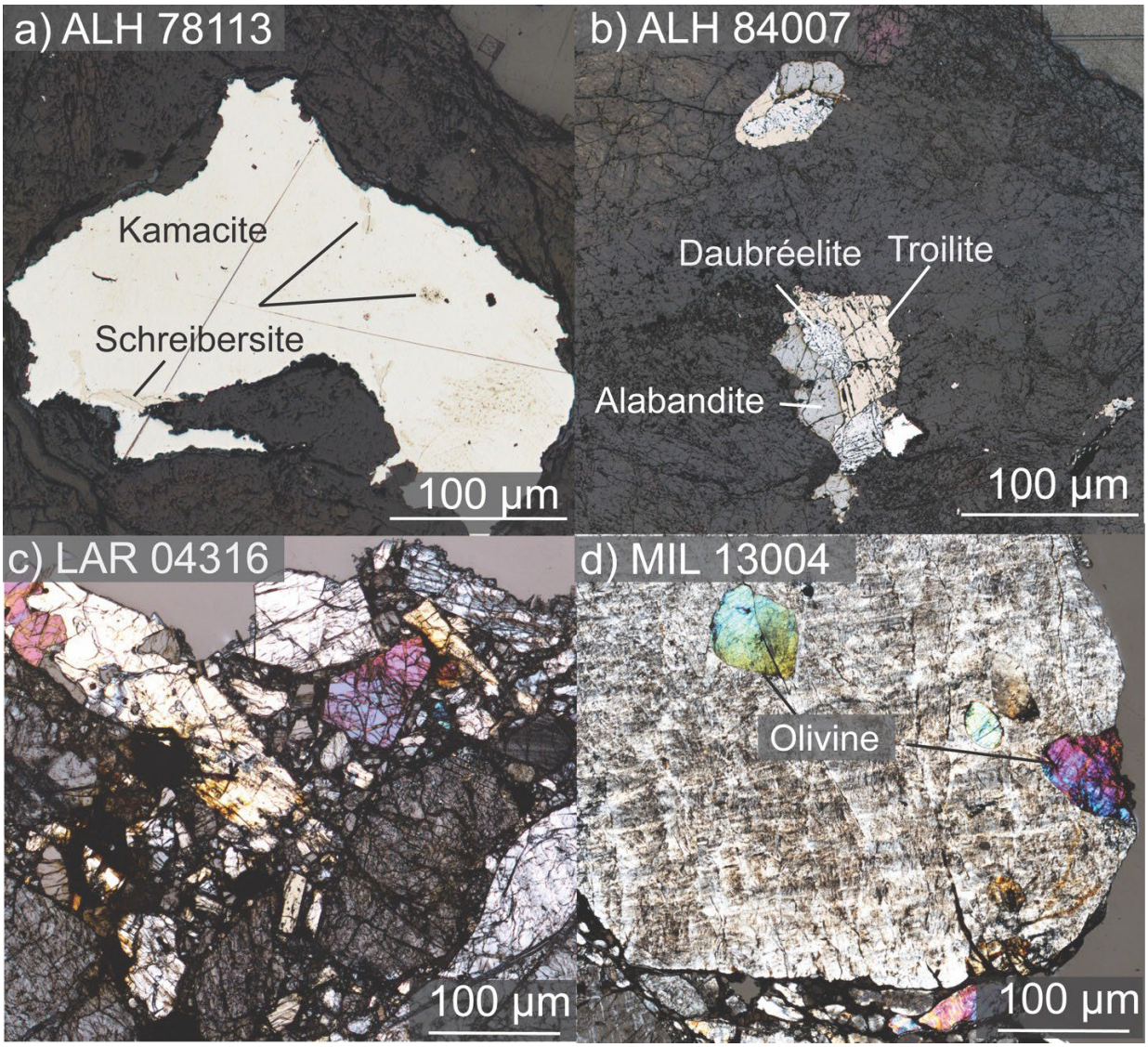

Figure

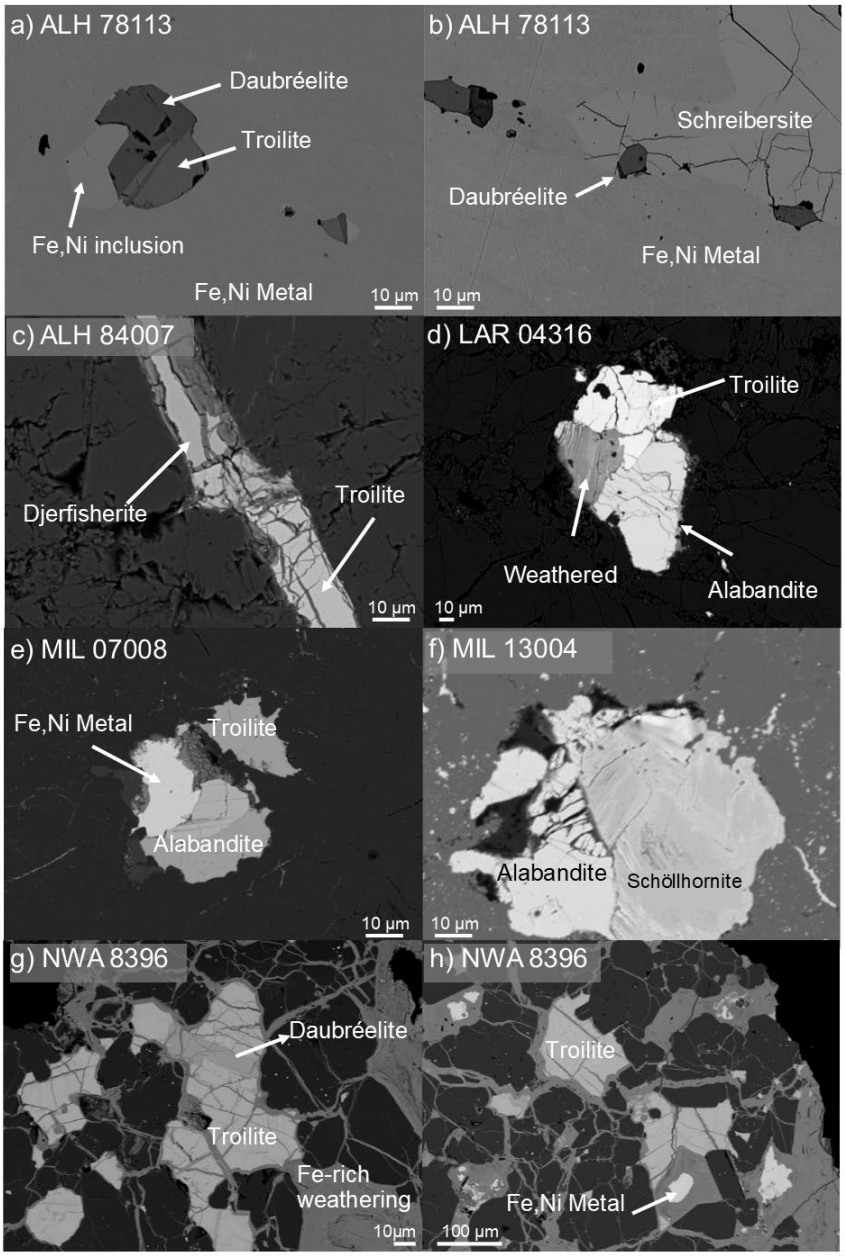
a) ALH 78113
Daubréelite
Troilite
Fe,Ni inclusion
Fe,Ni Metal
10 µm
b) ALH 78113
Schreibersite
Daubréelite
Fe,Ni Metal
10 µm
c) ALH 84007
Djerfisherite
Troilite
10 µm
d) LAR 04316
Troilite
Weathered
Alabandite
10 µm
e) MIL 07008
Fe,Ni Metal
Troilite
Alabandite
10 µm
f) MIL 13004
Alabandite
Schöllhornite
10 µm
g) NWA 8396
Daubréelite
Troilite
Fe-rich
weathering
10µm
h) NWA 8396
Troilite
Fe,Ni Metal
100 µm

Figure33

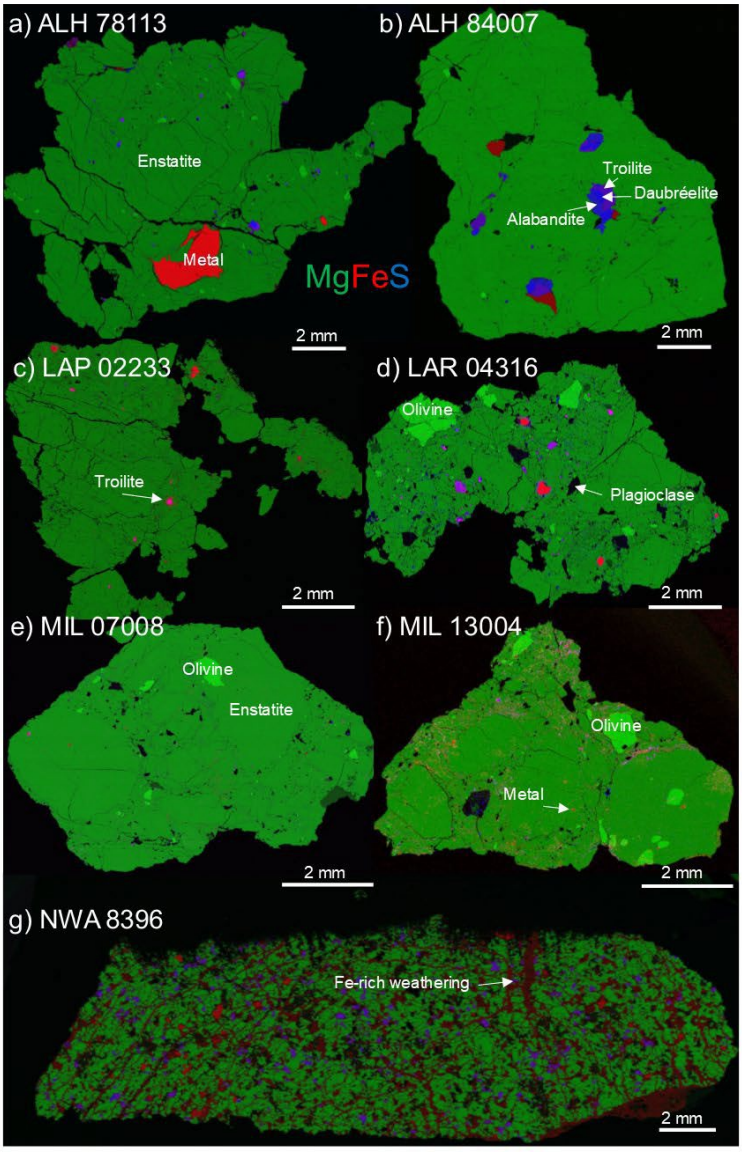
a) ALH 78113
Enstatite
Metal
MgFeS
2 mm
b) ALH 84007
Troilite
Daubréelite
Alabandite
2 mm
c) LAP 02233
Troilite
2 mm
d) LAR 04316
Olivine
Plagioclase
2 mm
e) MIL 07008
Olivine
Enstatite
2 mm
f) MIL 13004
Olivine
Metal
2 mm
g) NWA 8396
Fe-rich weathering
2 mm

Figure

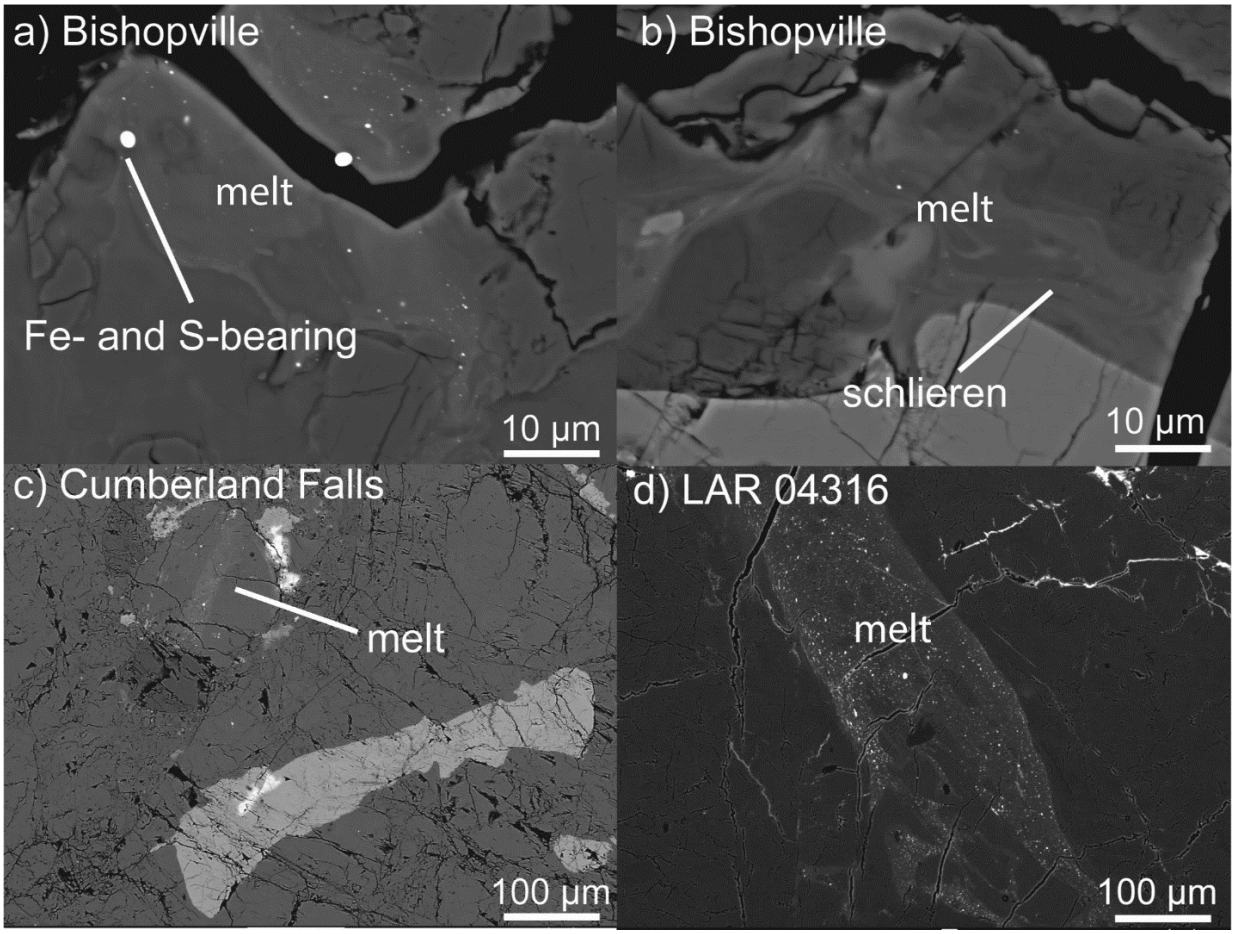
a) Bishopville
melt
Fe- and S-bearing
10 µm
b) Bishopville
melt
schlieren
10 µm
c) Cumberland Falls
melt
100 µm
d) LAR 04316
melt
100 µm

Figure

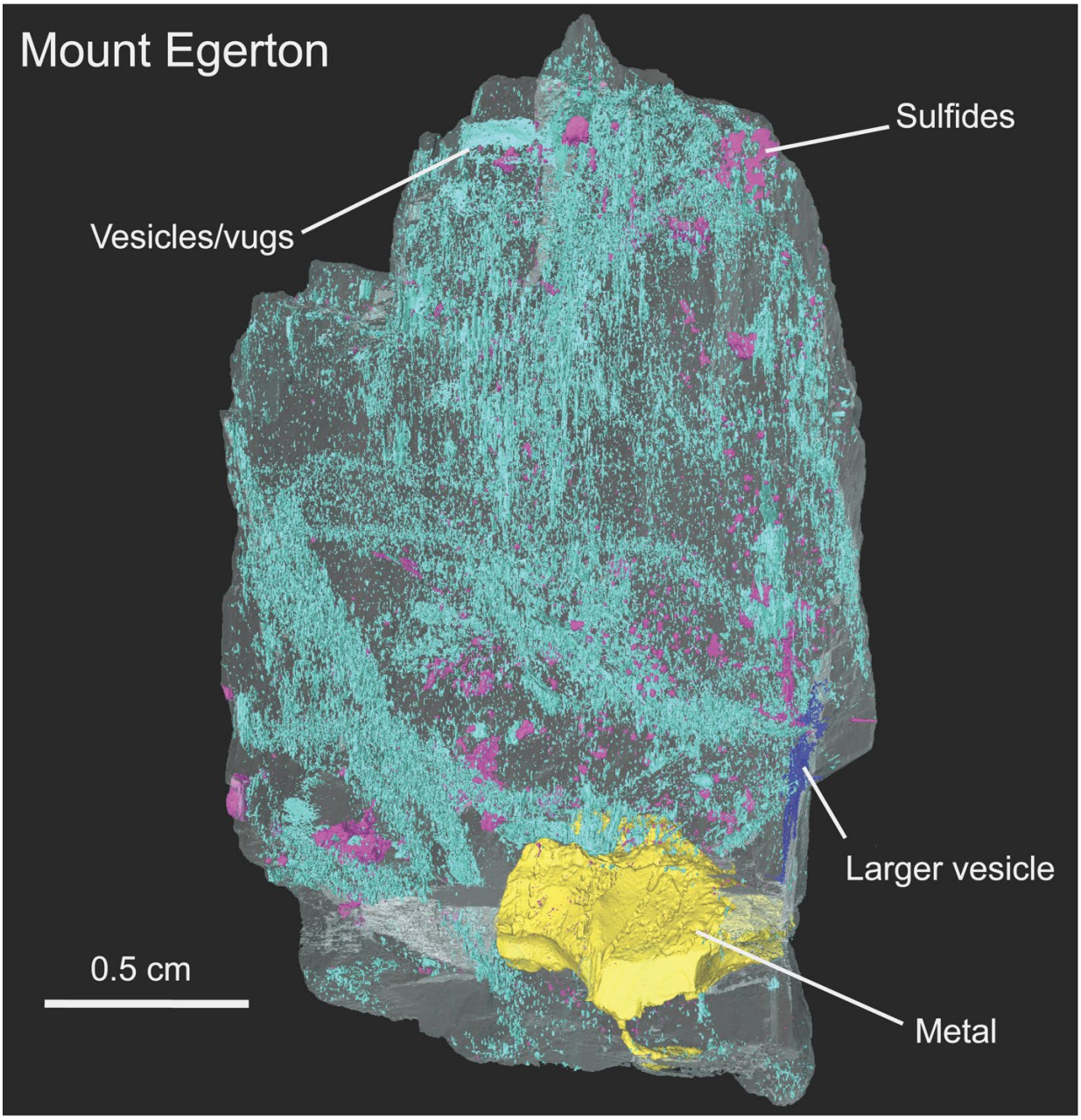
Mount Egerton
Sulfides
Vesicles/vugs
Larger vesicle
0.5 cm
Metal

Figure 6

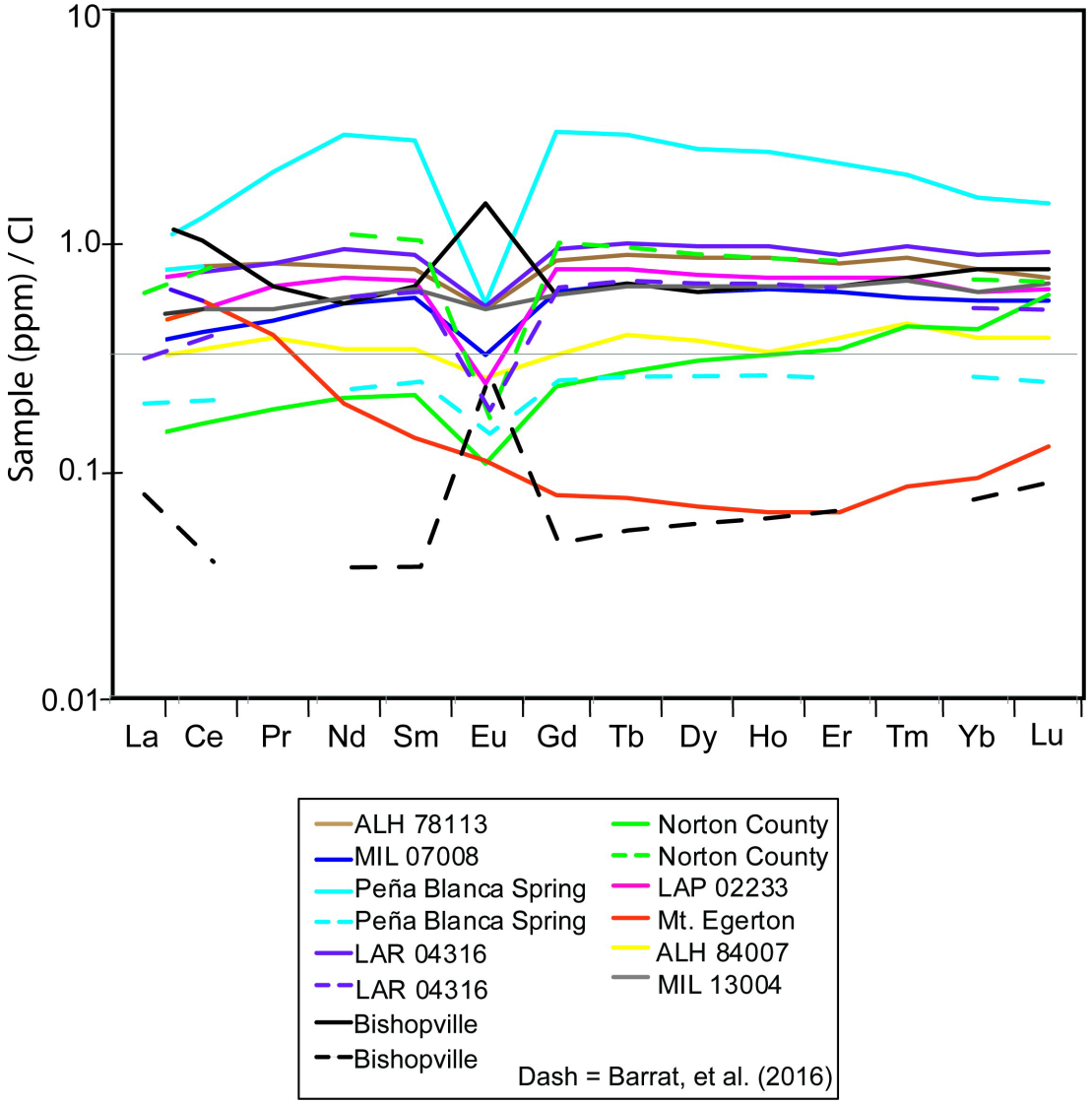
10
1.0
0.1
0.01
Sample (ppm) / CI
La
Ce
Pr
Nd
Sm
Eu
Gd
Tb
Dy
Ho
Er
Tm
Yb
Lu
ALH 78113
MIL 07008
Peña Blanca Spring
Peña Blanca Spring
LAR 04316
LAR 04316
Bishopville
Bishopville
Norton County
Norton County
LAP 02233
Mt. Egerton
ALH 84007
MIL 13004
Dash = Barrat, et al. (2016)

Figure

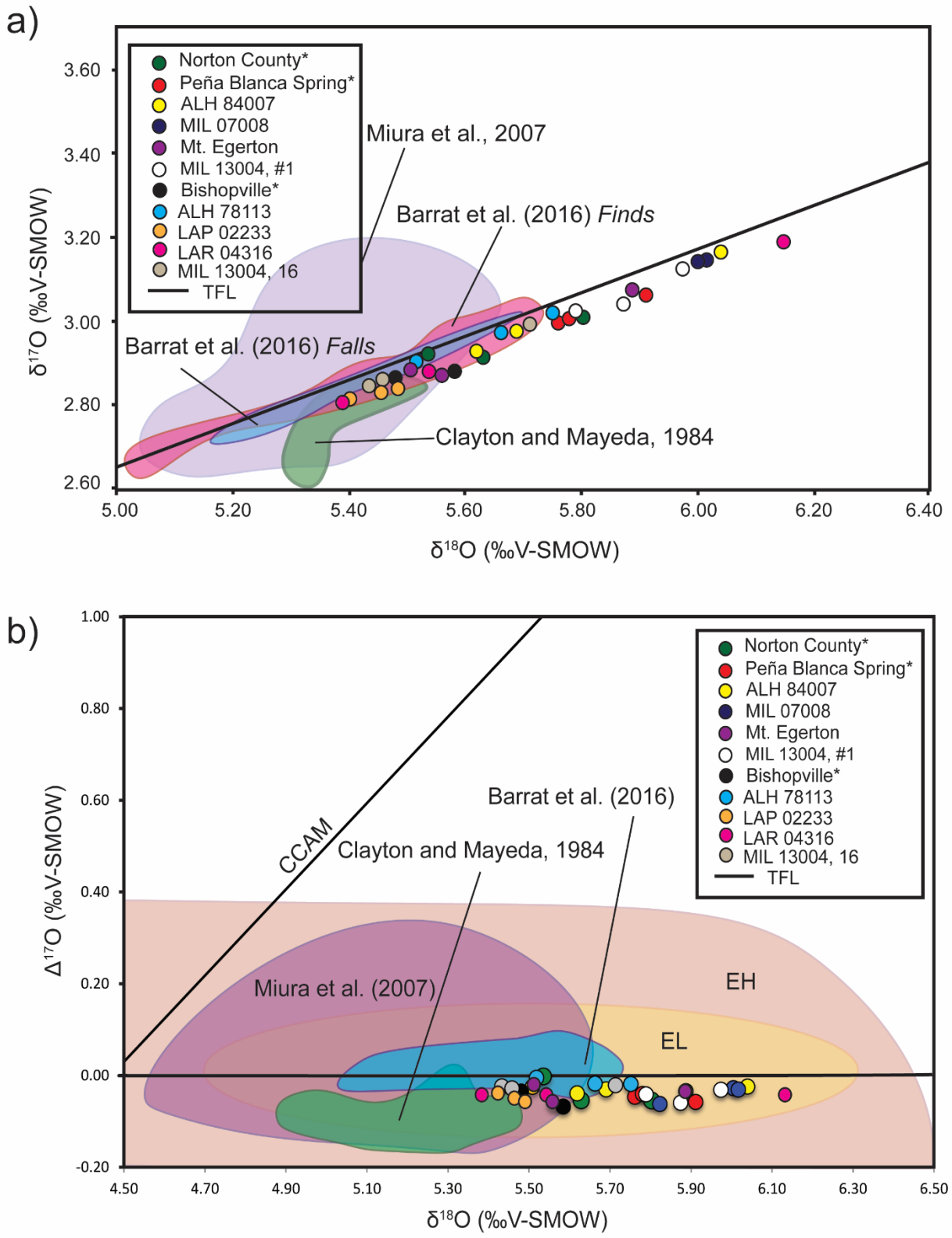
a)
Norton County*
Peña Blanca Spring*
ALH 84007
MIL 07008
Mt. Egerton
MIL 13004, #1
Bishopville*
ALH 78113
LAP 02233
LAR 04316
MIL 13004, 16
TFL
Miura et al., 2007
Barrat et al. (2016) Finds
Barrat et al. (2016) Falls
Clayton and Mayeda, 1984
δ17O (‰V-SMOW)
δ18O (‰V-SMOW)
b)
CCAM
Clayton and Mayeda, 1984
Barrat et al. (2016)
Miura et al. (2007)
EH
EL
Δ17O (‰V-SMOW)
δ18O (‰V-SMOW)

Figure 8

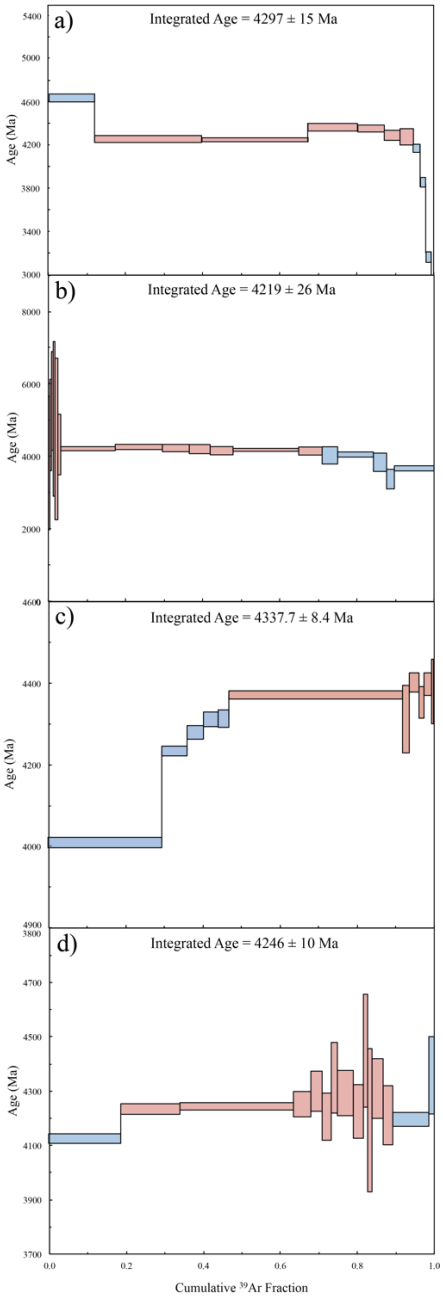
a)
Integrated Age = 4297 ± 15 Ma
b)
Integrated Age = 4219 ± 26 Ma
c)
Integrated Age = 4337.7 ± 8.4 Ma
d)
Integrated Age = 4246 ± 10 Ma
Age (Ma)
Cumulative ^{39}Ar Fraction

Figure 9

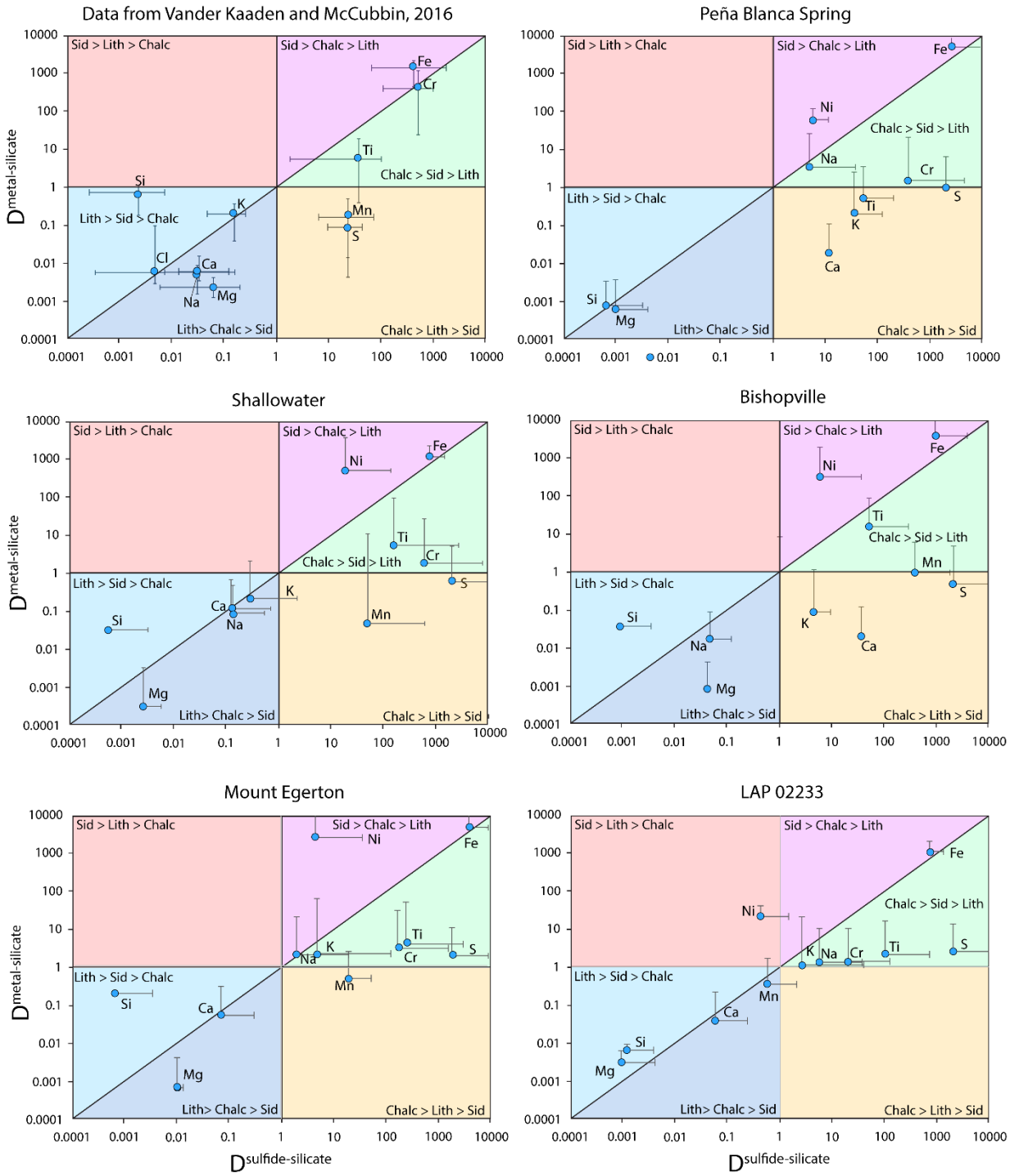
Data from Vander Kaaden and McCubbin, 2016
Peña Blanca Spring
Shallowater
Bishopville
Mount Egerton
LAP 02233
Sid > Lith > Chalc
Sid > Chalc > Lith
Chalc > Sid > Lith
Lith > Sid > Chalc
Lith> Chalc > Sid
Chalc > Lith > Sid
Dmetal-silicate
Dsulfide-silicate